Astronomy & Astrophysics manuscript no.
(DOI: will be inserted by hand later)

April 30, 2002

Penumbral structure and kinematics from high-spatial-resolution observations of Ca II K*

L.H.M. Rouppe van der Voort

The Institute for Solar Physics of the Royal Swedish Academy of Sciences, SCFAB, SE-10691 Stockholm, Sweden
e-mail: rouppe@astro.su.se

Received 8 March 2002 / Accepted 23 April 2002

Abstract. High-spatial-resolution spectra of the Ca II K line obtained with the Swedish Vacuum Solar Telescope (SVST) on La Palma are used to study the penumbra of a sunspot. The observed radiation temperatures in the Ca II K wing are used to derive the temperature stratification of fine-structure elements in the penumbra. It is found that in general, over the observed atmospheric depth range, penumbral structures keep their relative brightness identity with respect to their local surroundings, i.e., bright (dark) structures in the lower photosphere remain bright (dark) in the upper photosphere. Hot structures have a larger temperature difference between the bottom and the top of the photosphere than cool structures. Three semi-empirical atmosphere models, a cool, hot and mean model, are presented as being representative for the temperature stratification of penumbral fine structure. The mean temperature distribution of the centre-side penumbra is found to be up to 50 K hotter in the higher photosphere as compared to the limb-side penumbra. Hot structures being more numerous in the centre-side penumbra can account for this difference. These are primarily found near the outer penumbral boundary. It is suggested that the asymmetry can be explained by a differential line-of-sight effect that is caused by isotherms in bright structures having in the higher photosphere a tilt angle of approximately 7° with the horizontal, pointing downward towards the outer boundary. Line blends in the extended Ca II K wing are selected to study the Evershed effect and its height dependence. At a number of locations, the Evershed effect is found to be concentrated in channels which have a tendency to coincide with dark filaments. A weak correlation between brightness and velocity signal is found but also a number of bright structures with a significant Evershed signal. Simple numerical tests of flow channels in the penumbral atmosphere are performed to confront existing theoretical models with the observations. From these experiments it is found that the bulk of the flow must be concentrated in the lower atmospheric layers, i.e., below 200 km, and must have a velocity not higher than 6 $\mathrm{km\,s^{-1}}$. A channel width of 200 km is found to give the best reproduction of the observed velocities, so that the flow is either concentrated in a single channel or in a bundle of narrower channels. No direct indication is found of the Evershed channels being elevated above the continuum, and it is estimated that the flow channels reach down to at least 50 km above the continuum.

Key words. sunspots – Sun: photosphere – Techniques: spectroscopic – Techniques: high angular resolution

1. Introduction

Being the most eye-catching surface structure on the visible solar disk, sunspots have been studied for hundreds of years with ever improving spatial resolution. Like everywhere on the solar surface, sunspots harbour fine-structure to the smallest observable scales (for reviews see Muller 1992; Sobotka 1997). The sunspot penumbra is very rich in this respect and provides ample small scale structures. The intricate structuring of the penumbra containing different dynamical processes, like e.g., persistent flows, poses challenges for theoreticians and observers alike.

In the sunspot penumbra, the structuring is along bright and dark elongated filaments which have a typical length of 0″.5–2″ and a width of 0″.35 (Sobotka 1997). It has been argued that the true widths of penumbral filaments remain unresolved in present day observations (Sánchez Almeida & Bonet 1998), which led Sánchez Almeida (1998) to the conjecture that the penumbra consists of fibrils with width sizes as small as 1–15 km. Recently, Sütterlin (2001) challenged this concept from the analysis of spatial power spectra of a high resolution, speckle-reconstructed sunspot image. It was found that the power spectrum of the penumbra is enhanced over

* Based on observations made with the Swedish Vacuum Solar Telescope which was operated on the island of La Palma by the Royal Swedish Academy of Sciences in the Spanish Observatorio del Roque de los Muchachos of the Instituto de Astrofisica de Canarias.

$0\farcs3$–$0\farcs6$ which supports the idea that penumbral filaments have preferred widths of about 250 km.

From the intensities varying on small spatial scales in high-resolution observations, it can be inferred that the physical parameters that describe the underlying atmospheric columns vary on these small scales too. For the penumbra, relatively few attempts have been undertaken to determine these depth-depending physical quantities, like, e.g., temperature and density. The two-component model of Kjeldseth Moe & Maltby (1974) was one of the first attempts that provided temperature as function of optical depth in dark and bright penumbral filaments. For a long time, this was the only available penumbral atmosphere model and served as input for theoretical modelling of the penumbra (e.g., Montesinos & Thomas 1997). Del Toro Iniesta et al. (1994) applied an inversion technique to a series of high-resolution filtergrams scanning a magnetically insensitive Fe I line to study the temperature and velocity structure of the penumbral atmosphere. Besides the temperature and velocity stratifications, Westendorp Plaza et al. (2001b,a) derived the magnetic field stratification of a sunspot from inversions of observations of magnetically sensitive Fe I lines with a spatial resolution of approximately $1''$.

The narrow filamentary nature being one important characteristic of the penumbra, its dynamic nature is another. Of the many dynamical processes that shift and deform the observed spectral line profiles, the Evershed effect (Evershed 1909) is most important. The Evershed effect is observed in photospheric spectral lines as asymmetric line profiles and line-core shifts that indicate the presence of an outflow over a substantial part of the penumbra. For recent reviews on the Evershed effect the reader is referred to Muller (1992); Thomas (1994); Maltby (1997); Wiehr (1999). A selection of established observational properties are: (1) Depending on the observation angle, typical observed velocities can be as high as 6 $\mathrm{km\,s^{-1}}$. (2) The direction of the Evershed flow has very high inclination angle with respect to the surface normal so that the flow is nearly horizontal. (3) The magnitude of the Evershed signal increases towards the outer penumbral boundary. (4) Line cores of stronger photospheric spectral lines show lower Doppler shifts than weaker lines. The asymmetries for the strongest lines are essentially concentrated in the outer wings. The last property can be interpreted as the flow having decreasing velocity with height. Degenhardt (1993) pointed out, however, that if the penumbral volume that carries the flow decreases with height, an increasing velocity with height could still result in line profiles that are consistent with the observations.

The distribution of the Evershed effect over the penumbra is filamentary in nature (see e.g., Title et al. 1993; Johannesson 1993; Shine et al. 1994; Rimmele 1995). Apparently, certain filaments carry the bulk of the flow. Beckers (1968) claimed that the Evershed shift is concentrated in the darker structures. From then on, conflicting observations have appeared in the literature. The success or failure to confirm the brightness/velocity relationship is often attributed to the level of spatial resolution achieved in the observations. There is, however, a surprising inconsistency between high resolution data from tunable filter instruments and spectrographs: whereas filtergram studies confirm the association of the Evershed effect with dark filaments (Title et al. 1993; Shine et al. 1994; Rimmele 1995), several spectroscopic studies have failed to confirm this correlation (e.g., Wiehr & Stellmacher 1989; Lites et al. 1990; Johannesson 1993).

Theoretical models of the Evershed effect have been reviewed by Thomas (1994). Presently, two detailed models are most successful in explaining a number of observational properties: the siphon-flow model as proposed by Montesinos & Thomas (1997), and the moving-tube model by Schlichenmaier et al. (1998a,b). Montesinos & Thomas (1997) elaborated on the idea of Meyer & Schmidt (1968) that the flow is driven by a gas pressure difference between the footpoints of a thin magnetic flux tube in magnetohydrostatic equilibrium. As opposed to the static nature of the siphon-flow model, Schlichenmaier et al. (1998b) developed a dynamical two-dimensional model of a thin magnetic flux tube that acts as a convective element in a superadiabatic and magnetized penumbral atmosphere. As the tube convectively rises to the surface, a pressure gradient builds up locally and drives a gas flow along the tube. In this scenario, penumbral grains are identified as the hot upflow locations where the gas reaches the (optical) surface.

In this article, the temperature stratification in the penumbra of a full-grown sunspot is presented from inversions of high-spatial-resolution Ca II K spectra. The relatively simple formation mechanism of the Ca II K wings enable a fast and simple inversion technique so that a large number of spectra can be analysed. The extended nature of the wings provides a large number of depth grid points and the presence of a number of line blends makes it possible to probe velocities at different heights in the atmosphere. In this study, line-core shifts of these blends are employed to study the height dependence of the Evershed effect in the penumbra.

The outline of this article is as follows: in Sect. 2 the observations and instrumentation are described, followed by a description of the data reduction in Sect. 3. The inversion method to derive the temperature stratification from the Ca II K wing observations is discussed in Sect. 4. In Sect. 5 the results from the inversion are discussed and the temperature stratification of penumbral fine structure is presented. In Sect. 6 the selection of line blends for studying the Evershed effect is discussed and the results are compared with the theoretical models. A summary of the results and conclusions are presented in Sect. 7.

2. Observations and instrumentation

The leader sunspot in NOAA Active Region 8704 was observed on 20 September 1999 (S19.2°, E31.5°, $\mu = 0.77$) and 22 September 1999 (S20.0°, E4.0°, $\mu = 0.88$) with the Swedish Vacuum Solar Telescope (SVST) at La Palma

(Scharmer et al. 1985). NOAA/USAF classified AR8704 as being of magnetic class β (Mount Wilson magnetic classification) and as "Cso" in the 3-component McIntosh sunspot classification system (McIntosh 1990). The diameter of the studied sunspot was slightly more then $30''$ and the umbra was totally surrounded by a penumbra which contained a non-radial component. This particular sunspot was observed with other instruments using different techniques by Balthasar et al. (2001) and Sobotka & Sütterlin (2001) on the 20th of September, and by Schlichenmaier & Collados (2002) on later dates in September.

The observations comprise spectra of the Ca II K (3933.66 Å) line, slit-jaw images recorded with a 3 Å bandpass interference filter centered on the Ca II K line core and reference images recorded with a 12 Å bandpass interference filter centered on the G-band (4305 Å).

The images were stabilized using the correlation tracker (Shand et al. 1995) in quad-cell mode using the sunspot as tracking target. Differential image motion due to seeing effects alters the location of the slit on the Sun on a time scale of milliseconds. Therefore, spectrum-slit-jaw image pairs were recorded strictly simultaneously to allow for correlation between spectrograms and slit-jaw images.

On-line frame selection (Scharmer & Löfdahl 1991) was applied to select the best quality image from a burst of images. For the spectrum-slit-jaw pairs the image quality computation was performed on a selected subsection of the spectrogram. The CCD camera recording the G-band images was controlled by a separate workstation.

The short Littrow spectrograph is equipped with an holographic grating with 2400 lines mm^{-1} and has a theoretical spectral resolution of 500,000 (Scharmer et al. 1985). Operating with a 25 μm wide slit, the spectral resolution is slit-limited which corresponds to a bandpass of 30 mÅ at the wavelength of Ca II K. Spectrograms were recorded with a Kodak MegaPlus 1.6 BluePlus CCD camera which has a quantum efficiency of approximately 30% at the wavelength of the Ca II K line. The pixel size of 9 μm corresponds to approximately 11 mÅ in the spectral direction and $0\farcs083$ in the spatial direction. This provides a sampling of 2.7 pixels over the spectrograph bandpass. At an effective aperture of 47.5 cm, the diffraction limit of the telescope is $0\farcs2$ at 3933 Å. The spatial resolution was seeing limited and the effective spatial resolution of the presented spectrograms was estimated to range between $0\farcs3$ and $0\farcs8$, with the bulk having a resolution better than $0\farcs5$. The spectral range was 3923.7 – 3940.3 Å, covering a significant fraction of the wings of the Ca II K line. The exposure time for the spectrograms was 350 ms. The signal-to-noise ratio of the spectra before Fourier filtering was estimated to be 85 in the outer Ca II K wing.

The slit is a Cr-coated glass plate on which a 25 mm long and 25 μm wide ($0\farcs23$) slit is etched. The effective slit length was decreased so that the CCD chip was not fully illuminated. The remaining bands below and above the spectrograms were used to estimate the diffuse scattered light level in the spectrograph.

The slit plate had an off-axis tilt of a few degrees to direct the light to the imaging optics containing the Ca II K slit-jaw camera, G-band camera and correlation tracker camera. Slit-jaw images were recorded with a Kodak MegaPlus 1.4 CCD camera with a lumogen coating for enhanced UV sensitivity (quantum efficiency at Ca II K is $\sim 15\%$). The slit-jaw camera operated at approximately 1:1 magnification compared to the spectrograms but with a smaller pixelsize: 6.8 μm.

Parts of the presented data were recorded with the telescope in scanning mode. During this observation mode, the image of the sunspot is moved stepwise over the spectrograph slit in a direction perpendicular to the slit thereby creating a three-dimensional data cube with one spectral and two spatial dimensions. During a scan the correlation tracker locks the telescope on the sunspot target by keeping an image of the sunspot inside a reference box. After recording a spectrogram and slit-jaw pair, the correlation tracker camera is moved over a length corresponding to one slit width on the Sun ($0\farcs23$). This results in a displacement of the target with respect to the reference box and the correlation tracker sends a correction signal to the telescope tip-tilt mirror M3. Hereby the field of view of the telescope is effectively moved one slit width over the target and a new frame-selection image burst is started.

3. Data reduction

Data reduction and analysis were performed using the data processing software package and language ANA (Shine 1990).

3.1. Spectra and slit-jaw images

The reduction of the spectra followed the methods described by Kiselman (1994) with some changes and additions.

Flat fields were constructed from bursts of 50 added exposures with the telescope scanning randomly over an area around disk centre. In this way spatial information from the Sun is effectively removed from the resulting spectrogram. Spectral features were removed by dividing each spectrum by the mean spectrum of the whole spectrogram. The mean spectrum was constructed from addition of all spectral rows taking the slight curvature of the slit image into account. Spectra affected by dust specks were excluded. The final master flat field that was used for the correction of the individual spectrograms was constructed from 5 such frames and is therefore the result of addition of 250 exposures.

This mean spectrum was used for wavelength calibration using the spectral atlas of solar disk-centre intensity of Brault & Neckel (1987) (see Neckel 1999). The wavelength calibration of each individual spectrogram was performed by calibrating the mean spectrum of each spectrogram to the mean spectrum of the flat field.

After dark frame subtraction and flat field division, the spectrograms were corrected for diffuse scattered light from the spectrograph. The diffuse scattered light level was estimated from the signal at the CCD chip that was not directly illuminated by the slit and subtracted from each spectrum.

The noise level in the spectrograms was suppressed by application of a Fourier filter technique (Brault & White 1971) that resulted in an improvement of nearly a factor 2 in the signal-to-noise ratio (i.e., S/N $\sim$ 170 in the outer Ca II K wing).

After flatfielding the slit-jaw images, the individual slit-jaw images were co-aligned to their spectrogram companions by cross-correlation of two intensity profiles of the area covered by the slit. From the spectrogram, the spatial intensity profile was derived from a convolution of the spectrogram with the transmission profile of the slit-jaw filter. The intensity profile from the slit-jaw image was recovered from reflections from the slit glass plate (i.e., at the location of the slit).

3.2. Sunspot maps

Maps of the sunspot were constructed from the spatial-spectral data cube that was created by a scan over the sunspot. In 26 minutes the whole sunspot was covered in 151 scan positions. Image rotation due to the alt-azimuth design of the telescope turret was negligible during this time interval (rotation angle was less than 1°). Maps that were constructed from the data cube include intensity maps in the Ca II K wing, line-core intensity and line-core shift maps of weak line blends in the Ca II K wing (examples of six such Doppler maps are shown in Fig. 14) and temperature maps from inversions of the Ca II K wing (see Fig. 7). Although image jitter was decreased by the correlation tracker, a residual image shift remained from spectrogram to spectrogram. This was corrected for by determining the shift between two subsequent spectrograms through cross-correlation of the intensity signals from spatial cuts through the outer Ca II K wing, where spatial contrast is largest. The set of shifts that was derived in this way was applied to the construction of all maps. The maps shown in Fig. 7 and Fig. 14 were expanded in the scan direction to derive a uniform square pixel. In these figures, the slit is directed along the horizontal axis with the first scan position being at the top.

The image of the slit is slightly curved and introduces a relative shift between the spectra from one spectrogram (less than 0.8 pixel peak-to-peak). The exact sub-pixel shift for each spectral row on the CCD chip was determined from the flatfield spectrograms where all spatial information is smeared out and the spectral lines have a sufficient signal-to-noise ratio to allow for an accurate line-core-position determination. For the Doppler shift measurements, the determination of the line-core position was corrected for this curvature by subtracting the relative shift.

4. Inversion technique

The method to derive models of the upper photospheric regions from the damping wings of the Ca II K line basically follows the procedure developed by Shine & Linsky (1974). They showed that, based on a number of reasonable assumptions on line formation and atmospheric structure, the temperature stratification of an observed atmosphere can be derived from the observed radiation temperatures at different wavelength positions in the damping wings of the Ca II resonance lines. Depth spacing is measured as column mass density which is related to the wavelength displacement from the line core. This method has been used to derive atmosphere models of photospheric faculae (Shine & Linsky 1974), and late-type stars (Ayres et al. 1974; Ayres & Linsky 1975).

In the following, the inversion method is discussed starting from basic principles. After formulation of a simplified expression for the opacity in the Ca II K wing using modern atomic data, the validity of a number of assumptions is discussed that enables the inversion of the observed radiation temperatures.

For the damping wings of the Ca II K line, the line extinction coefficient can be formulated as:

$$\alpha_{\Delta\lambda} = \frac{e^2\lambda_0^4}{m_{\rm e}4\pi c^3}\, f_{lu}\, N_{\rm H} A_{\rm Ca}\, [\gamma_{\rm rad} + \gamma_{\rm vdW}]\, \frac{1}{\Delta\lambda^2} \qquad (1)$$

with $\Delta\lambda$ the wavelength displacement $(\lambda - \lambda_0)$ from line core λ_0 and $N_{\rm H}$ the hydrogen number density. Symbols for natural constants have their usual meaning: e and $m_{\rm e}$ are the electron's charge and mass respectively, and c is the speed of light. Atomic data for Ca II K was obtained from the VALD data base (Piskunov et al. 1995; Kupka et al. 1999; Ryabchikova et al. 1999), using for natural broadening a value of $\log(\gamma_{rad}) = 8.207$ (Theodosiou 1989) and for the oscillator strength $f_{lu} = 0.637$ (Theodosiou 1989). For the solar calcium abundance, a value of $A_{\rm Ca} = 2.29 \cdot 10^{-6}$ (Grevesse & Sauval 1998) was used.

Using the broadening cross-section for singly ionized calcium calculated by Barklem & O'Mara (1998), van der Waals broadening was approximated by:

$$\gamma_{\rm vdW} = \Gamma_{\rm W} \left(\frac{T}{5000{\rm K}}\right)^{0.39} N_{\rm H} \qquad (2)$$

with $\Gamma_{\rm W} = 1.33 \cdot 10^{-8}$, and between parentheses the temperature T normalized to 5000 K.

Even in the strong magnetic field of a sunspot, broadening due to the Zeeman effect is negligible in the wings of the Ca II K line.

The derivation of this simplified expression of the line extinction coefficient is based on the assumptions that in the temperature range where the wings of the Ca II K line are formed, the correction for stimulated emission is close to unity and the Ca II ground state is the dominating energy state. The latter assumption is supported by Fig. 1 where two contribution functions to the intensity in the wing are drawn in a plot of the population density of the Ca II ground state. The population density

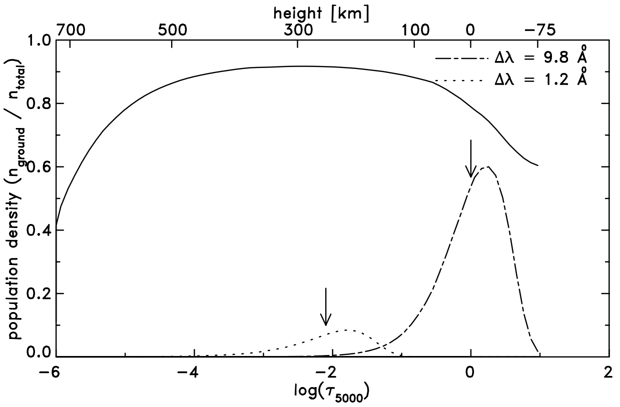

Fig. 1. Population density of the Ca II ground state in HolMul. The dotted and dash-dotted lines are the contribution functions to the intensity (on an arbitrary scale) for two locations in the wing (3932.46 Å and 3923.86 Å respectively, the two extrema in the inversion method). The arrows mark the mean height of formation.

and contribution functions (following Magain 1986) were computed using the radiative transfer computer program MULTI (Carlsson 1986) version 2.2, solving the non-LTE radiative transfer for a 6 level model of the calcium atom in the Holweger–Müller model atmosphere (Holweger & Müller 1974, hereafter HolMul). For the lowest and hotter parts of the photosphere, where the outer wings are formed, the ground state is not the only dominating energy state. This is one of the sources of uncertainty that makes results from the far wing less reliable as compared to smaller wavelength displacements from line core.

With Eq.(1), the observed wing intensities can be related directly to the atmospheric densities using the following assumptions:

a. The Eddington-Barbier approximation $I^+_\lambda(0,\mu) = S_\lambda(\tau_\lambda = \mu)$.
b. LTE holds for the formation of the Ca II K damping wings. This assumption is supported by Fig. 2 where the level populations for the K line transition are very close to the LTE populations in the part of the atmosphere that is relevant for the formation of the wing. The formation of the inner wings and line core is dominated by non-LTE effects and are omitted from the analysis. In the HolMul atmosphere, the depth range governed by the part of the wing between the two extrema where LTE is applicable spans approximately 260 km, ranging from $\log(\tau_{5000}) \approx -0.05$ for $\Delta\lambda \approx 9.5$ Å to $\log(\tau_{5000}) \approx -2.1$ for $\Delta\lambda \approx 1.2$ Å. With the LTE approximation the source function is equated to the Planck function and thereby the outgoing observed intensity is directly related to the local kinetic temperature.
c. $N_{\rm He} = 0.10\, N_{\rm H}$.
d. $N_{\rm e} \ll N_{\rm H}$ so that the gas pressure equals the total pressure in the region of formation.
e. Hydrostatic equilibrium holds. Whereas this is a widespread assumption when constructing semi-empirical atmosphere models, in the presence of strong magnetic fields (like in sunspots) it can be expected that magnetic forces due to gradients and tension contribute significantly to the force balance. Section 4.2 gives a discussion of possible implications.

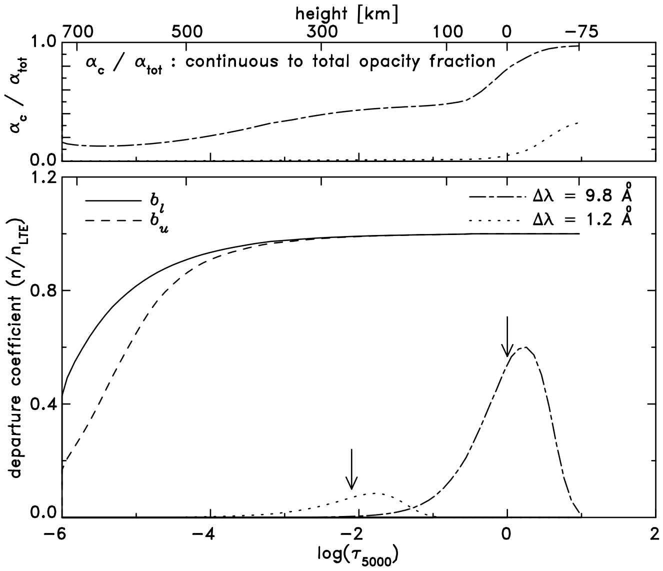

Fig. 2. The bottom panel shows the departure coefficients for the lower (b_l, full line) and upper level (b_u, dashed) of the Ca II K transition in HolMul. Like in Fig. 1 two contribution functions are over plotted on an arbitrary scale. The top panel shows the continuous opacity relative to the total opacity for the two selected wing positions.

Using the hydrostatic equilibrium equation and the relation $\mathrm{d}\tau = -\alpha \mathrm{d}h = -\kappa\rho \mathrm{d}h$, the local gas pressure can be computed by

$$P_{\rm gas}(\tau_\lambda = \mu) = \int_{h(\tau=0)}^{h(\tau=\mu)} g\rho \mathrm{d}h = \int_{\tau=0}^{\tau=\mu} \frac{g}{\kappa_\lambda}\, \mathrm{d}\tau_\lambda \qquad (3)$$

with κ_λ the mass extinction coefficient and g gravitational acceleration. If natural broadening were the only relevant broadening agent, κ_λ is independent of both temperature and density and drops out of the integral. For the damping wings of the Ca II K line van der Waals broadening is however dominating and we approximate the integral with a simple one-point quadrature: $q_\lambda\, \mu g/\kappa_\lambda$. The quadrature weight q_λ was empirically determined to have a value of 1.6, based on evaluating the integral in Eq.(3) in a range of model atmospheres.

Using the perfect gas law, we obtain for the Ca II K line the following relation for $N_{\rm H}$ in the region of its formation:

$$N_{\rm H} = \frac{1}{2}\left(\frac{5000}{T}\right)^{0.39}\left[-\frac{\gamma_{\rm rad}}{\Gamma_{\rm W}} + \left\{\left(\frac{\gamma_{\rm rad}}{\Gamma_{\rm W}}\right)^2 - \frac{4g\mu\mu_{\rm mol}m_{\rm H}}{A_{\rm Ca}\Gamma_{\rm W}k}\,\frac{m_{\rm e}4\pi c^3 q_\lambda}{e^2 f_{lu}\lambda_0^4}\left(\frac{T}{5000}\right)^{0.39}\frac{\Delta\lambda^2}{T}(1-\tau_{\rm c})\right\}^{1/2}\right] \qquad (4)$$

where k is Boltzmann's constant, $\mu_{\rm mol}$ the mean molecular weight, and $m_{\rm H}$ hydrogen mass. The factor $(1-\tau_{\rm c})$ is a correction for continuous opacity. For $\Delta\lambda \gtrsim 8$ Å the continuous extinction reaches the same order of magnitude as the line extinction and this correction term becomes non-negligible. That is illustrated in the upper panel of Fig. 2 where for two wing positions the fraction of the continuous to total opacity is drawn. Since the continuous extinction of the observed atmosphere is not known a priori, the uncertainty in probing the density distribution increases with increasing distance from the line core. Realistic values for $\tau_{\rm c}$ were inserted, which were derived from inversions on model atmospheres where the continuous opacity is known. The uncertainty for the deeper photospheric layers can be decreased even more by doing a forward computation of the Ca II K line profile and a fit to the observed profile by altering the atmospheric parameters in the deepest layers. This method is described in Sec. 4.1.

Using the hydrostatic equilibrium assumption, the column mass density $m = \int \rho \, {\rm d}h$ is related to the gas pressure (see Eq.(3)) and can computed using Eq.(4) and (c):

$$m = 1.1\, N_{\rm H} kT/g \tag{5}$$

and the temperature stratification is obtained as temperature being a function of column mass density.

In Fig. 3 the crosses mark the temperature distribution derived from an inversion of a synthetic line profile calculated in the HolMul atmosphere. We see that for the deeper layers, corresponding to wavelength positions in the far wing, the deviation from the input atmosphere (full line) grows due to the uncertainty in the continuous opacity. Moreover, for the deeper layers a non-negligible fraction of the calcium atoms populate other levels than the Ca II ground state.

4.1. Extrapolation

The observed photons in the far wing are not exclusively formed in a narrow region around $\tau = \mu$ but carry information about the deeper layers of the atmosphere. To fully exploit the diagnostic value of the wings and to decrease the uncertainty in the method described above, the derived atmosphere can be extrapolated to deeper layers by using a fitting procedure. First, the deepest atmosphere points, most affected by the uncertainty in the continuous opacity, are cut out and replaced by a conservative linear extrapolation of a set of depth points above. The extrapolation is extended to a column mass density corresponding to $\tau_{5000} \approx 2$. The top of the atmosphere is extended with a few grid points by linear extrapolation of a set of grid points in the top layer of the atmosphere.

Subroutines from the computer program MULTI (version 2.2) (Carlsson 1986) are used to compute other atmospheric parameters (in LTE) like electron and hydrogen number density and the τ_{5000} scale, important for synthetic line formation. Given the temperature and column mass density derived from the analytical inversion method and starting sets of hydrogen populations and electron number density, an iteration procedure is started to solve hydrogen radiative transfer (LTE) and the equation of hydrostatic equilibrium consistently. A synthetic Ca II K line profile is computed from the resulting atmosphere and compared with the observed line profile. If the agreement between synthetic and observed profiles is not satisfactory, the temperatures for the deepest grid points are raised monotonically and the procedure to the equation of hydrostatic equilibrium is restarted. This iteration scheme is continued until the radiation temperatures in the wing match the observed radiation temperatures within 1%.

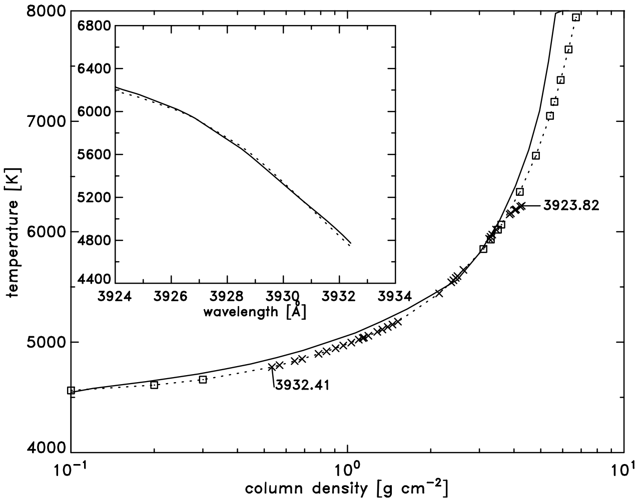

Fig. 3. Temperature distribution for the HolMul atmosphere (solid line). Crosses mark the $T(m)$ distribution derived from an inversion of a synthetic Ca II K line profile. For the two extrema the corresponding wavelengths are denoted. Squares mark extra grid points derived from extrapolation. The dotted line is the resulting atmosphere from which a line profile is calculated. The radiation temperatures of this profile (dotted) and of the synthetic profile from the model atmosphere (full) are shown in the inset.

The dotted line in Fig. 3 shows the temperature distribution after extrapolation of the atmosphere derived from a synthetic line profile from the HolMul atmosphere under an observing angle of $\mu = 1$. The squares mark the added grid points. A line profile was calculated from this derived atmosphere, shown in the inset together with the original line profile. The maximum deviation in radiation temperature is less than 40 K. For the deepest grid points, the strong deviation in kinetic temperature from the original atmosphere mostly comes from the error in column density. In this example, the deepest grid points of the derived atmosphere are cooler than the original atmosphere because of the fact that the grid points around 0.8 g cm^{-2} are slightly hotter. The outer Ca II K wing is most sensitive to these depth points and the slight overestimation of the temperature in this region is compensated for by lower temperatures in deeper layers.

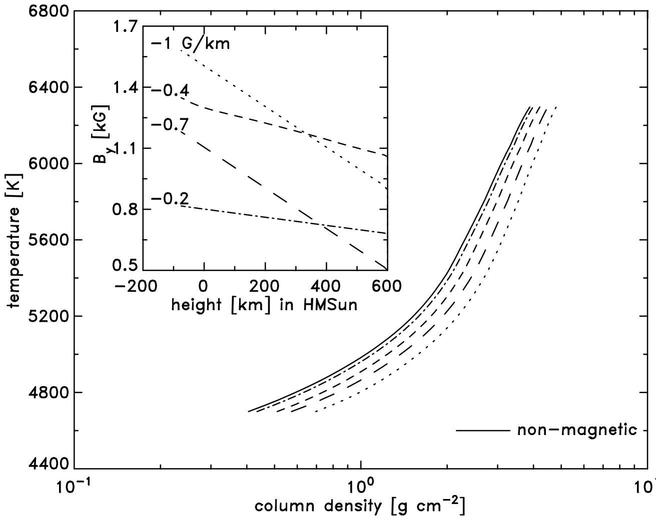

Fig. 4. Temperature as function of column mass density derived from atmospheres with different magnetic field strength distributions. Radiation temperatures are equal for all atmospheres. The small inset shows magnetic field strength B_y as function of height. The number left of each line is the field strength gradient (in G km^{-1}).

4.2. Hydrostatic equilibrium

A common assumption when constructing semi-empirical atmosphere models is the validity of hydrostatic equilibrium. In a sunspot, however, strong magnetic fields are present that can be expected to contribute significantly to the total pressure. Especially in the penumbra, where the magnetic field is strongly inclined with respect to the surface normal (see e.g., Title et al. 1993), magnetic forces are likely to play an important role in the vertical component of the momentum equation. Since observations of the three-dimensional height dependent magnetic field vector on sub-arc second scales are presently unavailable, we have to restrict ourselves to reasonable assumptions on the field strength and configuration to estimate the effect of the magnetic field on the force balance.

Analogue to Eq.(4) we can formulate an expression for the hydrogen number density as sampled by the Ca II K wings with a correction term that accounts for the magnetic field gradient. After adding the magnetic pressure term $B_y^2/(8\pi)$ to the left-hand side of Eq.(3), the integration of this term over the atmosphere column may be approximated by the difference in B_y^2 between $\tau \ll 1$ and $\tau = \mu$. Now, the column mass density can be calculated from a modified version of Eq.(5):

$$m = (1.1\, N_{\rm H} kT - \frac{\Delta B^2}{8\pi})/g \qquad (6)$$

where ΔB^2 stands for the approximation of the integral $\int {\rm d}B_y^2$.

Introducing a magnetic field in a non-magnetic atmosphere leads to the evacuation of the atmosphere and therefore to a decrease in the number density. To reach optical depth unity in such an atmosphere, more absorbers are needed since the opacity in the Ca II K wing is dominated by van der Waals broadening. In a magnetized atmosphere we can expect the Ca II K wing to sample a larger column density than in a non-magnetic atmosphere for equal radiation temperatures.

To estimate the effect of the magnetic field on the results from the inversion of observed Ca II K line profiles, different magnetic field distributions were seeded in a model atmosphere. From a given Ca II K line profile (calculated from the non-magnetic atmosphere), temperature distributions are calculated for the different cases. The magnetic field distributions, shown in the inset of Fig. 4, represent possible penumbral distributions. The magnetic field gradient $\mid \partial B/\partial z \mid$ is estimated to be around 1 G km^{-1} in the penumbra (Solanki 2001). The short dashed distribution follows the law: $B = 1300 + 50 \log \tau$, adopted from Martínez Pillet (2000).

The solid line in Fig. 4 shows the temperature distribution with no magnetic field present. The other four temperature distributions are significantly affected by the presence of magnetic field. In extreme cases, the error, expressed in temperature, could be larger than 200 K.

With no high-resolution measurements of the magnetic field configuration presently available, the use of the hydrostatic equilibrium assumption in this (and other) work should be considered as a first order approximation to derive the temperature stratification of the penumbral atmosphere.

4.3. Calibration

To obtain radiation temperatures from the observations, the spectra were calibrated to a reference spectrum. The HolMul model atmosphere for the quiet sun was used as reference atmosphere from which the reference spectrum was computed. The HolMul atmosphere is well known to reproduce the solar spectrum in LTE and is therefore a natural choice when modelling the weak line blends in the Ca II K wing as described in Sect. 6. Furthermore, this model atmosphere was selected because it produces the best fit for the wings of a synthetic Ca II K line profile to an atlas profile (Brault & Neckel 1987) in comparison to the models HSRA (Gingerich et al. 1971) and VAL3C (Vernazza et al. 1981).

The atlas spectrum was taken from the spectral atlas of solar disk-centre intensity of Brault & Neckel (1987). Note that due to the high density of spectral lines, an unambiguous definition of the solar continuum shortward of 4020 Å is impossible. For the atlas, the local continuum below 4420 Å is estimated by polygonal tracks connecting local maxima and is, as the authors fully acknowledge (see Neckel & Labs 1984), subject to personal arbitrarinesses. The two tracking points that define the continuum for the Ca II K line (3900 and 4000 Å) are far beyond the observed wavelength region and therefore a 'clean' wing point is used to normalize the computed spectrum. The arrow in Fig. 5 at 3924.3 Å marks the point in the wing

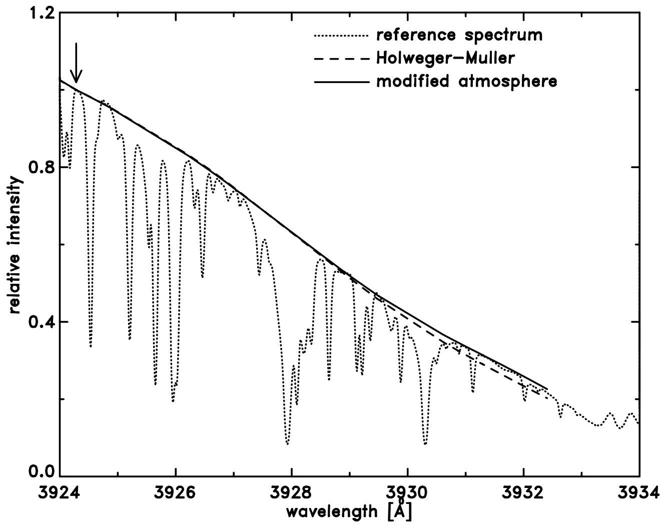

Fig. 5. Reference spectrum constructed from a large number of spectra outside the sunspot (dotted) relative to the intensity in the wing marked by the arrow. The dashed and solid lines are synthetic spectra computed from the HolMul atmosphere and the same atmosphere with higher temperatures in the upper photosphere.

that is used for normalization, this part of the wing is assumed not to be contaminated by weak line blends.

To obtain radiation temperatures from the observed spectra, a mean spectrum was constructed that was calibrated to a synthetic spectrum. This mean spectrum was constructed to resemble a quiet Sun profile by selecting only slit positions well outside the sunspot and excluding bright plage. Even though the slit reached up to 15″ outside the sunspot the constructed spectrum did not completely resemble a 'true' quiet Sun spectrum. Fig. 5 shows that the quiet synthetic spectrum is cooler for the inner wings ($\lambda \lesssim$ 3930 Å). A modified reference atmosphere with 1.5% higher temperatures for column densities lower than 1.2 $\mathrm{g\,cm^{-2}}$ results in a better fit for the inner wing (full line). For the actual temperature calibration only the outer wing ($\lambda >$ 3930 Å) was used.

4.4. Summary of sources of error

In this section, the magnitude of different sources of error in the inversion method are summarized. Noise is one of the minor sources of error in the temperature determination and accounts for a random scatter of approximately 10 K. The different wavelength positions in the Ca II K wing have a different level of interference with the wings of neighbouring line blends, which is partly due to smearing by the instrumental profile. For some of the wing positions, this is a major source of scatter in the temperatures, e.g., near $\lambda \approx$ 3931 Å, $m \approx$ 1.0 g cm^{-2} and $\lambda \approx$ 3930.6 Å, $m \approx$ 1.3 g cm^{-2}. This is a more systematic source of error with a magnitude of less than 20 K. Other systematic errors enter the inversion procedure through the limited validity of the assumptions, like e.g., the Eddington-Barbier approximation, neglecting depopulation of the Ca II ground state, neglecting contribution continuous extinction in outer wing, the approximation of the integral in Eq.(3) by a one-point quadrature, etc. Their impact on the final result is reduced by using the extrapolation procedure that aims at a best fit to the observed line profile. The error in the recovered radiation temperatures is less than 1% (less than 60 K).

Finally, as is discussed in Sec. 4.2, the use of the assumption of hydrostatic equilibrium bears a potential risk of introducing errors.

5. Inversion results

5.1. Temperature stratification in penumbra

The inversion was applied to all the spectra in the spectrograms that constitute the spot scan and to the spectra from high-quality spectrograms of September 22. The results from one such spectrogram recorded under excellent seeing conditions is shown in Fig. 6. The generally cooler penumbra clearly stands out against the hotter surroundings that includes bright (hot) plage at the left hand side. With the slit crossing the penumbral filaments at right angles in the mid-penumbra the temperature makes fluctuations on small spatial scales.

The two maps in Fig. 7 are constructed from the spot scan sequence and show the temperature at a fixed column density. The lower contrast in the map at lower column density can be attributed to a longer photon mean free path in higher atmospheric layers as compared to the deep photosphere so that temperature fluctuations are smeared out over larger spatial scales.

Histograms of the temperature distribution in the far and inner wing are well fitted by single Gaussians (see Fig. 8). This is in agreement with histograms of the penumbral intensity distribution from high-spatial resolution images (Grossmann-Doerth & Schmidt 1981; Denker 1998) from which it was concluded that a simple two-component model, i.e., two distinct classes of bright and dark filaments, is insufficient to describe the physics of the penumbra. Darkness and brightness of penumbral filaments is a relative measure that depends on the local surroundings.

When the two temperature distributions are plotted as scatter plots, the penumbra displays a markedly different temperature-height dependence than the quiet sun (bottom panels in Fig. 8). The elongated distribution for the penumbra shows the general characteristic that hot (cool) structures remain hot (cool) over the whole depth of the covered atmosphere range. This can also be inferred from Fig. 6 and Fig. 7 where in the latter the overall penumbral scene is similar in both temperature maps. This is in contrast to the photospheric granulation pattern in the quiet sun where the intensity distribution is inverted in the upper-photospheric atmosphere layers. The inverse granulation pattern is not obviously present in the lower right panel of Fig. 8 which could partly be due to the presence of plage. Furthermore, it is not clear whether this part

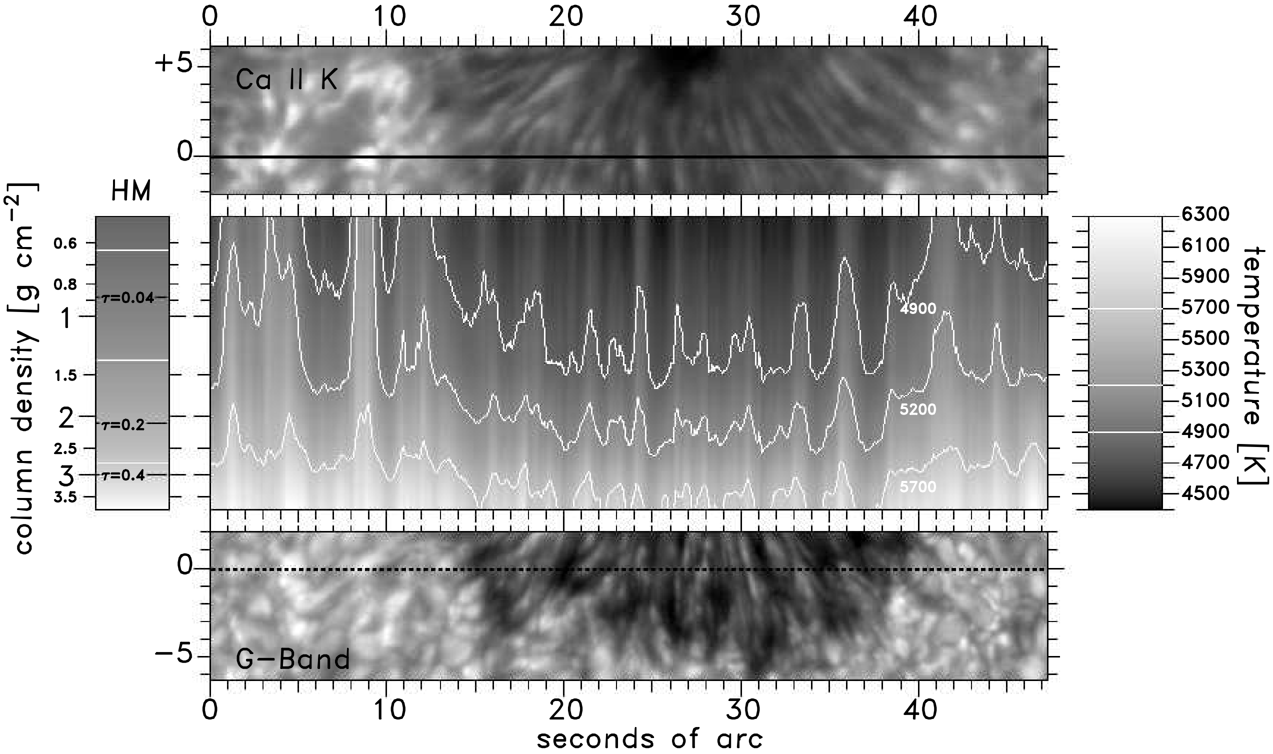

Fig. 6. The middle panel displays temperature as function of column mass density resulting from the inversion of one spectrogram. Temperature is indicated as levels in gray-scaling with the full range given at the right hand side. White contours mark three different temperature values. Depth is measured as column density along the vertical abscissa (logarithmic scaling). Along the horizontal runs spatial location along the slit with the accompanying Ca II K slit-jaw image shown above for a direct comparison with the top layers of the measured atmosphere range. The solid black line marks the slit location on the Sun. A quasi-simultaneous G-Band image is shown below with the dashed line marking the approximate location of the spectrograph slit. For comparison, the panel on the left marked with 'HM', shows the temperature distribution in the reference atmosphere HolMul with temperature contours and marked depths of different values of optical depth τ_{5000}.

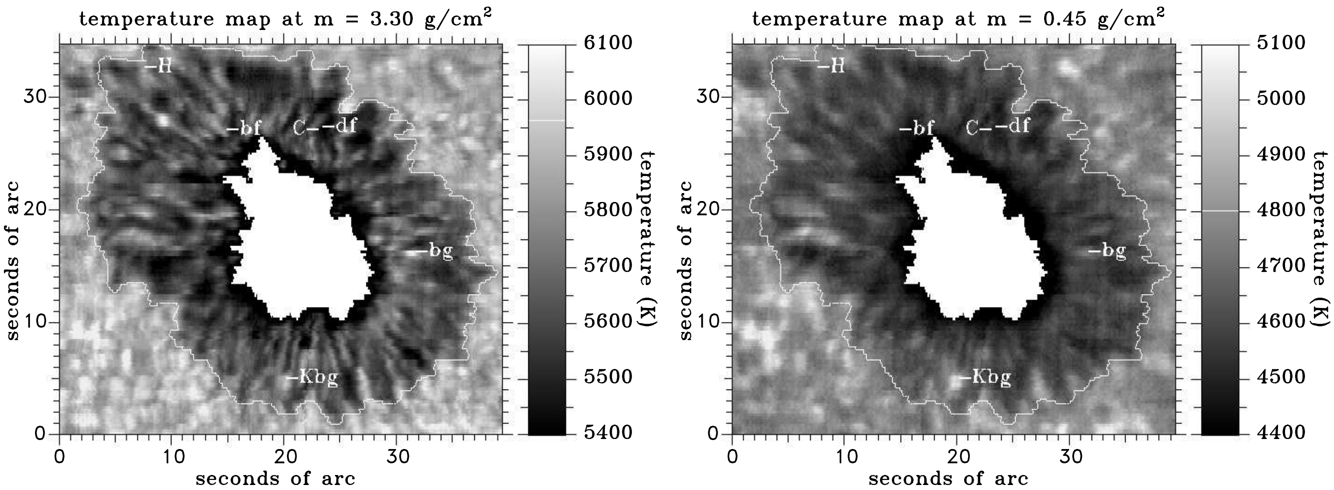

Fig. 7. temperature maps for different values of the column mass density. Each map is accompanied with a colour coded temperature scaling. The white line in this scaling box marks the temperature in the reference model atmosphere at this specific column density. *Left:* $m = 3.30\,\mathrm{g\,cm^{-2}}$, $\mathrm{T_{ref}} = 5966\,\mathrm{K}$, $\log(\tau_{5000}) = -0.3$. *Right:* $m = 0.45\,\mathrm{g\,cm^{-2}}$, $\mathrm{T_{ref}} = 4804\,\mathrm{K}$, $\log(\tau_{5000}) = -1.9$. The umbra is masked out (white) and the white contour marks the penumbral boundary. The labels refer to the example atmospheres shown in Fig. 9: *bf* = bright filament, *df* = dark filament, *bg* = bright grain, *Kbg* = Ca II K bright penumbral grain. *H* and *C* mark the model atmospheres tabulated in Table 1.

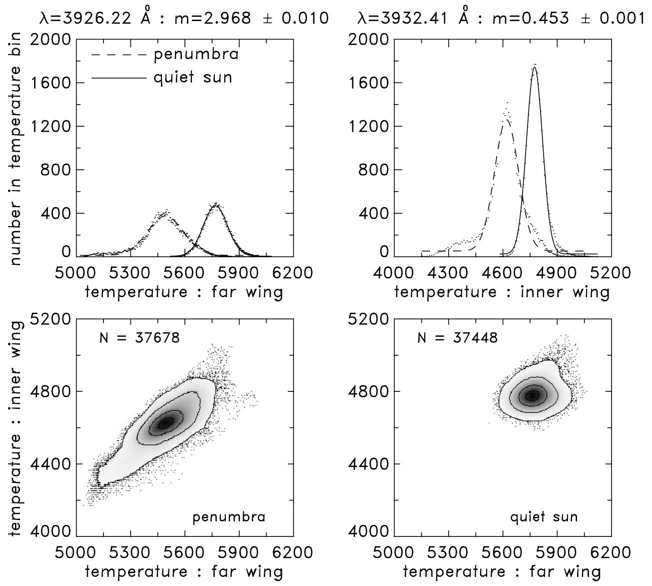

Fig. 8. The top two panels show histograms of the temperature distribution in the penumbra and quiet sun. At left is the radiation temperature measured in the far Ca II K wing at $\lambda = 3926.22$ Å, at right in the inner wing at 3932.41 Å. The two bottom panels show scatterplots of the two wing temperatures for the penumbra (left) and quiet sun (right). In the most crowded regions, contours and grayscaling mark the density of scatterpoints, with dark being most dense.

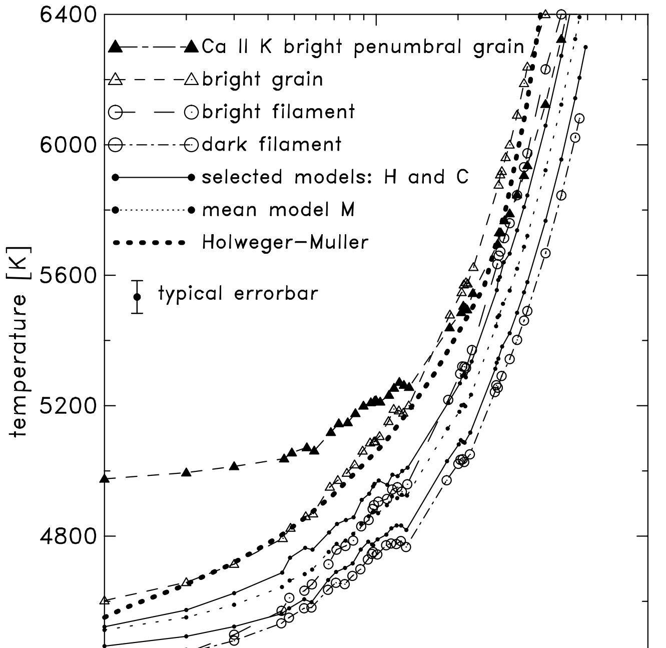

Fig. 9. Examples of the temperature distribution in the atmospheres of selected penumbral fine structure.

of the wing is probing high enough in the atmosphere to display the intensity inversion. However, when comparing broad-band (3 Å) Ca II K line filtergrams with G-band granulation images (see e.g., Fig 2 of Lites et al. (1999)), bright ridges in Ca II K can be found to overlay dark intergranular lanes in G-band.

The slope of the scatter points in the lower left panel of Fig. 8 shows the general trend in the temperature differences between bottom and top of the observed atmosphere range for penumbral fine structure. Hot structures have a larger temperature difference than cool structures which is displayed as a steeper curvature for the run of temperature versus column density.

An example of difference in $T(m)$-curvature is shown in Fig. 9: the bright filament has a temperature similar to the quiet sun in the bottom layers while it is about as cool as the dark filament in the higher layers of the atmosphere. Further examples of temperature distributions include a bright grain that is significantly hotter than quiet sun in the deeper photosphere while being as cool as quiet sun in the higher layers. The temperature distribution of what has been dubbed 'Ca II K bright penumbral grain' has a markedly different curvature: while being not particularly hot in the deep photosphere, it is significantly hotter higher up. Close inspection of the accompanying filtergrams reveals that this structure is particularly bright in the Ca II K filtergram but a modestly bright structure in the G-band image.

The three models drawn with solid lines in Fig. 9 are selected as representative penumbral models. From the whole set of penumbral atmospheres derived from the inverted spectra, only 11 % are hotter than model H and 11 % are cooler than model C. Model M is the mean model for the whole penumbra, resulting from an inverted Ca II K spectrum constructed from all spectra. These models are tabulated in Table 1. Presented are temperature T and column mass density m, for which the values of $0.3 < m < 3.1$ g cm^{-2} correspond to wavelength positions in the Ca II K wing. Grid points outside these boundaries result from the extrapolation procedure. The tabulated values for $\log(\tau_{5000})$ and height come from the MULTI computations (see Sect. 4.1). Height is defined in km above reference optical depth $\tau_{5000} = 1$.

5.2. Comparison with other work

A comparison of the mean penumbral model with other penumbral models in the literature is shown in Fig 10. Excellent agreement is achieved with the mean penumbral model of Del Toro Iniesta et al. (1994), especially in the lower atmosphere. Their mean model is constructed from a series of penumbral models derived from an inversion of high spatial resolution spectrofiltergrams in the Fe I 5576 Å line. The bright penumbral model of Kjeldseth Moe & Maltby (1974) has similar temperatures through most of the temperature range. Their model was derived from continuum measurements and parallel modifications to the HSRA model (Gingerich et al. 1971). The temperatures of their dark filament model are rather low but their values lie within the range of temperatures found in this

C				*H*				*M*			
m	T	$\log(\tau_{5000})$	z	m	T	$\log(\tau_{5000})$	z	m	T	$\log(\tau_{5000})$	z
0.10	4463	−3.10	443	0.10	4522	−3.10	445	0.10	4512	−3.10	444
0.20	4493	−2.61	374	0.20	4573	−2.62	374	0.20	4551	−2.61	374
0.30	4523	−2.32	332	0.30	4625	−2.32	331	0.30	4589	−2.32	332
0.45	4562	−2.02	290	0.45	4688	−2.02	288	0.45	4644	−2.02	289
0.48	4579	−1.97	283	0.48	4734	−1.97	281	0.48	4664	−1.97	282
0.54	4606	−1.87	269	0.55	4764	−1.87	267	0.55	4683	−1.87	268
0.58	4597	−1.83	263	0.58	4758	−1.82	260	0.58	4697	−1.82	261
0.67	4665	−1.72	248	0.67	4811	−1.72	244	0.67	4751	−1.72	246
0.71	4690	−1.67	240	0.72	4837	−1.67	237	0.72	4776	−1.67	238
0.77	4702	−1.61	232	0.77	4849	−1.61	228	0.77	4786	−1.61	230
0.82	4716	−1.56	225	0.83	4858	−1.56	221	0.82	4807	−1.56	223
0.88	4759	−1.51	218	0.88	4911	−1.50	213	0.88	4837	−1.51	215
0.93	4783	−1.46	211	0.94	4930	−1.46	206	0.94	4861	−1.46	208
0.97	4774	−1.44	207	0.97	4952	−1.43	202	0.97	4873	−1.43	204
1.01	4790	−1.40	202	1.02	4971	−1.39	197	1.02	4870	−1.40	199
1.09	4805	−1.34	194	1.10	4957	−1.34	188	1.10	4895	−1.34	191
1.14	4824	−1.31	189	1.15	4988	−1.30	183	1.14	4922	−1.31	186
1.19	4833	−1.27	184	1.20	4984	−1.27	178	1.19	4916	−1.27	181
1.24	4833	−1.24	180	1.25	5000	−1.24	174	1.24	4927	−1.24	176
1.29	4819	−1.21	175	1.30	5010	−1.20	168	1.30	4924	−1.21	171
1.82	5030	−0.94	136	1.84	5209	−0.93	128	1.83	5130	−0.93	131
2.01	5081	−0.86	124	2.03	5268	−0.85	116	2.02	5181	−0.86	119
2.05	5094	−0.85	122	2.07	5291	−0.84	113	2.06	5201	−0.84	117
2.09	5089	−0.83	120	2.11	5298	−0.82	111	2.10	5203	−0.83	115
2.12	5086	−0.82	118	2.14	5287	−0.81	110	2.13	5198	−0.82	113
2.22	5117	−0.78	112	2.25	5335	−0.77	103	2.23	5234	−0.78	107
2.74	5313	−0.61	87	2.78	5554	−0.59	77	2.76	5444	−0.60	81
2.78	5332	−0.61	85	2.81	5585	−0.58	75	2.80	5471	−0.59	80
2.82	5344	−0.59	84	2.85	5594	−0.57	73	2.84	5477	−0.58	78
2.91	5381	−0.57	80	2.95	5640	−0.54	69	2.93	5512	−0.56	74
3.10	5422	−0.52	72	3.10	5666	−0.49	62	3.10	5553	−0.51	66
3.50	5548	−0.41	56	3.50	5809	−0.38	46	3.50	5687	−0.40	51
4.20	5767	−0.25	32	4.20	6059	−0.18	21	4.20	5922	−0.22	26
4.80	5955	−0.11	14	4.80	6273	−0.02	2	4.80	6123	−0.07	7
5.40	6143	0.02	-3	5.40	6487	0.14	−15	5.40	6324	0.08	−10
6.20	6394	0.19	-23	6.20	6772	0.34	−37	6.20	6593	0.27	−30
7.50	6801	0.47	-52	7.50	7236	0.66	−68	7.50	7029	0.57	−60
8.50	7114	0.68	-72	8.50	7593	0.89	−89	8.50	7364	0.79	−81
9.50	7428	0.89	-91	9.50	7950	1.11	−109	9.50	7700	1.00	−101

Table 1. Selected semi-empirical penumbral atmosphere models. Tabulated physical quantities are: column mass density m [g cm^{-2}], temperature T [K], optical depth $^{10}\log(\tau_{5000})$ and height [km]. Temperature and column density are derived directly from the observations, optical depth and height are derived from the extrapolation procedure. The horizontal lines make the division between gridpoints corresponding to wavelength positions in the Ca II K wing ($0.3 < m < 3.1$), and gridpoints resulting from the extrapolation procedure. 11% of the atmosphere models in the sample are cooler than model C, 11% are hotter than model H, and model M is constructed from the mean penumbral spectrum.

work. The model from Westendorp Plaza et al. (2001b) is a mean over an azimuthal path across the penumbra, with the vertical bars indicating the range for paths from the inner penumbra to the outer penumbra (adapted from their Fig. 17). Their model is significantly cooler in the lower atmosphere which they attribute to the exclusion of brighter penumbral zones in the averaging procedure (when comparing with Del Toro Iniesta et al. (1994)). This model lies within the scatter of temperature distributions found in this work.

Like in the inversion method used in this work, all other atmosphere models have been derived using the assumption of hydrostatic equilibrium to hold. By doing that, the magnetic field configuration is assumed not to contribute to the force balance.

5.3. Limb-side / centre-side asymmetry

When comparing the mean temperature distributions for the centre-side penumbra with the limb-side penumbra, the centre-side penumbra is up to 50 K hotter at higher layers (see Fig. 11).

Analysing a sunspot observed under an angle $\mu = 0.88$ Del Toro Iniesta et al. (1994) found a similar difference

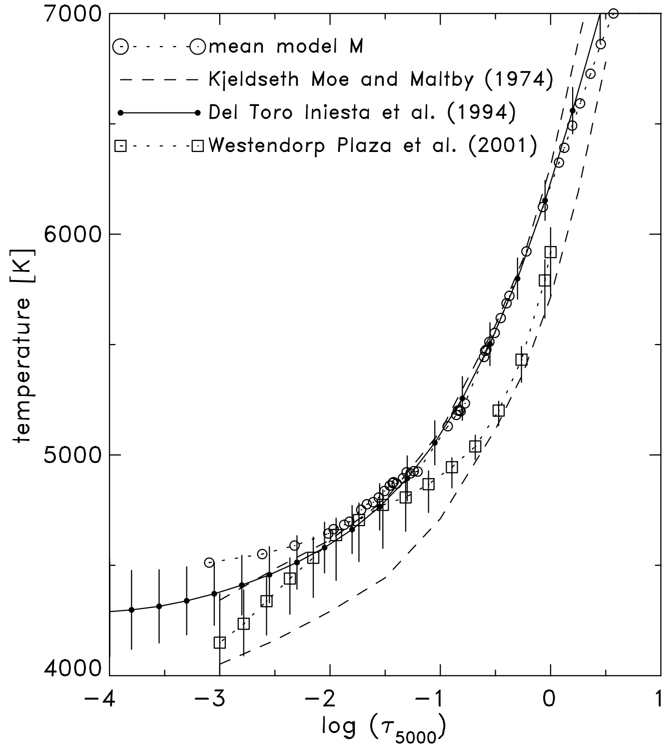

Fig. 10. Comparison of the mean model M with penumbral atmosphere models found in the literature. The dashed lines are the bright (upper) and dark filament models of Kjeldseth Moe & Maltby (1974). The solid line is the mean penumbral atmosphere of Del Toro Iniesta et al. (1994) with error bars being standard deviations. The dotted line with squares is the mean temperature in the mid penumbra from Westendorp Plaza et al. (2001b), r/R_p = 0.7, with the bars ranging from the inner penumbral model, r/R_p = 0.5, to the outer most model, r/R_p = 1.0.

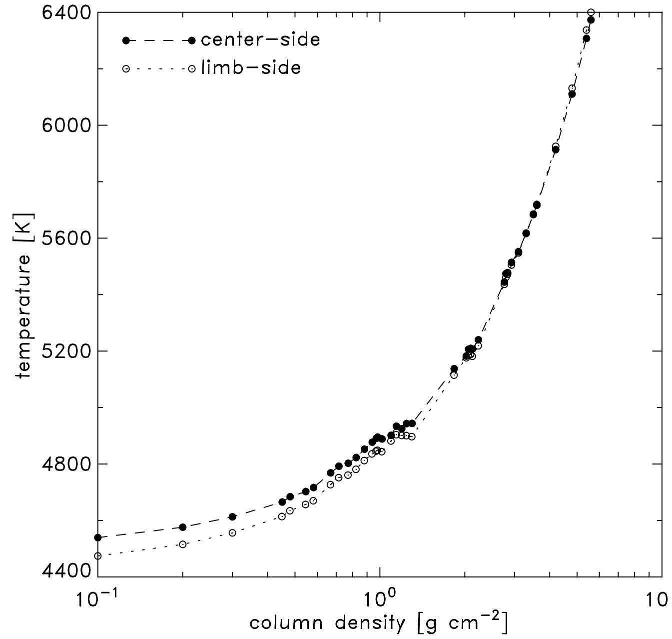

Fig. 11. Mean temperature distribution for centre-side and limb-side penumbra.

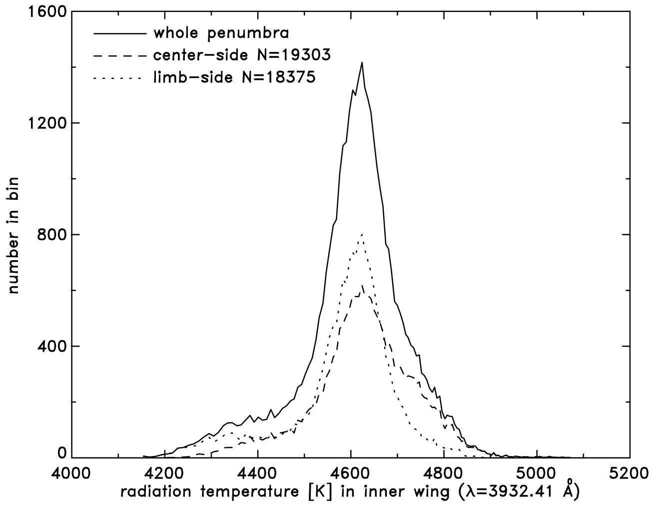

Fig. 12. Histograms of the inner-wing radiation temperature distribution in the penumbra (see upper right panel of Fig. 8) split into two histograms: one for the centre-side penumbra (long dash) and one for the limb-side penumbra (short dash).

when comparing mean models from centre-side and limb-side penumbra. The authors do not discuss this asymmetry but from their Fig. 4 and Table 1 it can be deduced that the mean models for the centre-side penumbra are generally hotter.

Differences between centre and limb-side penumbra have also been reported in measurements of the Evershed flow. Rimmele (1995) found a difference in the shape of spectral profiles originating from the limb and centre-side penumbra respectively. Line-core shifts in the centre-side penumbra were generally larger and line asymmetries from bisectors had their maximum deeper in the line in the centre-side penumbra than in the limb side. He concluded that this difference is most likely caused by a line-of-sight effect. Rimmele noted that unit optical depth is apparently reached at different geometrical depths in the two sides of the penumbra, and concluded that deeper atmospheric layers are observed in the centre-side penumbra.

Westendorp Plaza et al. (2001b,a) also found an centre/limb-side asymmetry in the observables. For the magnetic field, they found a more frequent occurrence of nearly horizontally oriented and even reverse-polarity fields on the limb side. For the Evershed flow, they found a more clear presence of strong downflows in the deepest layers of the penumbral photosphere on the limb side. This made them suggest that the geometrically deeper layers are probed on the limb-side penumbra, contrary to Rimmele.

To elaborate more on the observed asymmetry in the mean temperature found in this work, Fig. 12 shows the histogram of the radiation temperatures in the inner wing (dashed line in upper right panel of Fig. 8) split into a distribution for the centre side and one for the limb side. This reveals that the centre side has an excess of hot structures. It is the bright structures that cause the difference in the mean temperature between limb and centre-side in Fig. 11. These structures that appear to be hot in the inner Ca II K wing are mainly found at the outer penumbral boundary. The cool halves of the centre and limb-side histograms have similar distributions and mean temperature distributions constructed from these collections do not show any difference between the two sunspot sides. Histograms of the outer wing radiation temperatures are similar for centre and limb-side penumbra, both on the cool side as on the hot side of the distribution (not shown).

The asymmetry can be interpreted as a difference in the observing angle, or that in higher atmospheric layers, isotherms are tilted such that on the centre side deeper layers are probed (i.e., higher temperature) than on the limb side. The curvature of the sun over the sunspot diameter could account for a difference in the viewing angle of approximately 2°, which corresponds to a difference in the radiation temperature in the inner wing of only 10 K. Line profile computations at different observing angles show that a difference of 14° results in a temperature difference of approximately 50 K in the inner Ca II K wing. This suggests that at the outer penumbral boundary, bright structures have a tilt angle of approximately 7° with the horizontal, pointing downward toward the outer boundary. In such a geometry, deeper layers are probed on the centre-side than on the limb-side penumbra resulting in higher radiation temperatures observed in the inner Ca II K wing. Such a small tilt angle for the isotherms leads to a modest elevation on the vertical scale when the tilted region extends over several arcseconds on the outer part of the penumbra.

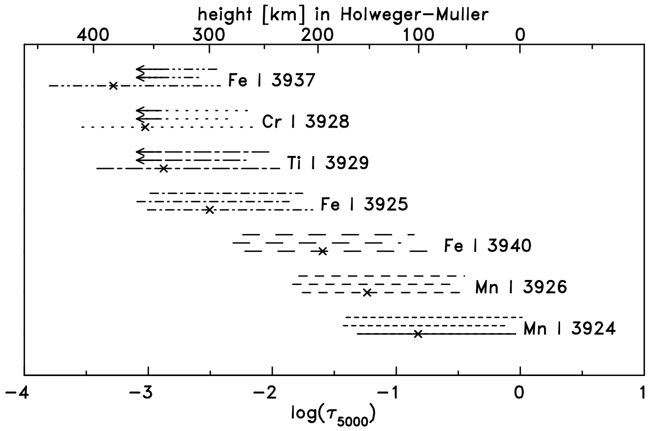

Fig. 13. FWHM of contribution functions to the line-core depression for different weak line blends in the Ca II K wing in three different atmospheres. For each spectral line, the bottom line is in the HolMul model atmosphere, with the crosses marking the mean height of formation of the line-core depression. The middle line is in the cold penumbral atmosphere C, the top in the hot penumbral H atmosphere. The arrows mark where the optical depth range is too shallow to cover a complete FWHM.

6. Evershed effect from line blends

6.1. Line modelling

From the set of observed line blends in the wing of the Ca II K line a subset of lines was selected to probe flow velocities at different heights in the penumbral atmosphere. The selection was based on detailed line modelling for each line including the computation of contribution functions for determination of the relevant formation depth range. Atomic data were obtained from the VALD data base (Piskunov et al. (1995); Kupka et al. (1999); Ryabchikova et al. (1999), detailed references in Table 2) and for each line a synthetic line profile was computed and compared to the atlas profile. For the radiative transfer LTE was assumed to hold and the HolMul atmosphere was used as model atmosphere. Partition functions for the different elements were taken from Gray (1992). To simulate the effect of macro-turbulence the synthetic line profiles were convolved with a radial-tangential function (Gray 1978) with a macro-turbulence velocity of 1.8 km s^{-1}. The $\log(gf)$ values were then altered until the line-core depression fitted the atlas spectrum. Table 2 summarizes the atomic data of the selected subset of lines that was used for further analysis. The lines were selected on basis of the quality of the atomic data, their applicability for Doppler shift measurements, i.e., well isolated, not contaminated by other lines and relatively strong, and their uniqueness of line-core height of formation so that the ensemble of lines probes material velocities at different heights (see Fig. 13).

The effect of hyperfine splitting for the two manganese lines was taken into account by computing the line profile as the composite of a number of components. The wavelength position and relative strength of the components were derived from laboratory spectra observed by Litzén (2001) (see Table 3).

Figure 13 shows the FWHM of the contribution functions to the line-core depression. Their ordering illustrates that the spectral lines are sensitive to bulk velocities in overlapping though complementing atmosphere regions and the complete set of lines covers a significant fraction of the accessible part of the atmosphere.

Besides the widths of the contribution functions in the HolMul atmosphere, Fig. 13 also shows the contribution function widths in the cold C and hot H penumbral atmospheres. Although the temperatures at equal optical depths differ up to a few hundred degrees, the FWHMs of the contribution functions do not differ dramatically: they are overlapping over a substantial fraction of their widths. Note that the optical depth scale is not absolute but only valid in each individual atmosphere. On an optical depth scale, the depth interval where the line cores are formed are roughly the same for the various fine-scale structures in the penumbra.

ion	wavelength[Å]	EP_{low}[eV]	$\log(gf)$	$\log(gf)^*$	$\log(\gamma_{vdW})$	$\log(\gamma_{rad})$	$\log(\gamma_{stark})$	height[km]
Mn I	3924.066	3.859[1]	−0.060[2]	−0.71[a]	−7.689[1]	8.149[1]	−5.360[1]	101
Fe I	3925.207	3.292[3]	−1.400[3]	−1.40	−7.172[6]	7.911[4]	−4.778[4]	283
Mn I	3926.475	3.844[1]	0.000[2]	−0.13[a]	−7.543[1]	7.977[1]	−4.966[1]	148
Cr I	3928.645	1.004[1]	−1.220[2]	−1.31	[b]	6.607[5]	−6.387[5]	341
Ti I	3929.874	0.000[5]	−1.060[2]	−1.13	[b]	7.818[5]	−6.198[5]	323
Fe I	3937.335	2.692[3]	−1.459[3]	−1.42	−7.757[6]	7.470[4]	−6.262[4]	369
Fe I	3940.039	3.415[4]	−2.013[4]	−2.03	−7.800[4]	8.201[4]	−6.217[4]	177

[1] Kurucz (1994c), [2]Martin et al. (1988), Fuhr et al. (1988), Kurucz (1993), [3] Nave et al. (1994), [4] Kurucz (1994b)
[5] Kurucz (1994a), [6] Barklem et al. (2000)
[a] hyperfine splitting see Table 3.
[b] detailed broadening cross sections are computed (Barklem et al. 1998)

Table 2. Summary of atomic data for selected line blends. The wavelength is the line-core wavelength in the atlas. EP_{low} is the excitation potential of the lower level. The $\log(gf)^*$ values result from the fit of the line core to the atlas. The height is the mean height of formation of the line-core depression in kilometers above $\tau_{5000} = 1$.

Mn I 3924		Mn I 3926	
$\Delta\lambda$ [Å]	strength	$\Delta\lambda$ [Å]	strength
+0.007	1.000	+0.015	1.000
-0.020	0.641	-0.015	1.000
+0.033	0.100		
-0.055	0.155		

Table 3. Hyperfine components for two Mn I lines. $\Delta\lambda$ is wavelength displacement relative to line core (see Table 2). Strength is relative to the main component.

6.2. NLTE effects

Since the formation heights of line cores are calculated with the assumption of LTE, deviations from the LTE level populations could result in errors.

Shchukina & Trujillo Bueno (2001) made a careful investigation of NLTE effects for the formation of Fe lines in the solar photosphere using a realistic atomic model. Over-ionization due to the hot near-UV radiation field was found to be an important mechanism causing a depopulation of the Fe I levels. A decreased departure coefficient for the lower excitation level of a transition results in an opacity deficit. This effect is important for the correlation of line-core Doppler shifts to material velocities at a specific height since it shifts the region of formation to lower atmospheric layers. The extent of this effect is highly dependent on the excitation potential and the atmosphere where the line is formed in: for an intergranular (cooler) atmosphere, the shift in formation height was found to be generally smaller than in a granular (hot) atmosphere. Following Shchukina & Trujillo Bueno (2001), the Fe I lines used in this study would be considered as being intermediate-excitation lines and the formation height would be overestimated by less than 50 km in the HolMul atmosphere which is intermediate between their granular and inter-granular models.

Note, however, that by adjusting the $\log(gf)$ values to fit the actual line depths of the atlas line profiles, the NLTE effects on the formation heights are reduced so that the error of 50 km can be considered as a conservative upper limit.

For the other lines, it should be noted that these are also from transitions of minority ionization stages, so that near-UV over-ionization is a likely candidate as being an important de-population mechanism. For these elements, no detailed studies of NLTE line formation in the solar atmosphere are known to the author, so it can only be surmised that the LTE formation heights are upper limits.

Given the limited extent of the formation height error for the Fe I lines, the corrective adjustment of the $\log(gf)$ values and the notion that for the cooler penumbral atmospheres the NLTE effects are reduced, it seems unlikely that the determined order of formation heights, i.e., that one spectral line is formed higher than another, is mixed due to NLTE effects.

6.3. Doppler shift determination

Asymmetries of the line profile have been regarded as an essential signature of the Evershed effect (Maltby 1964) and are clearly present in the data. However, in this study only the line-core Doppler shifts are used to probe velocities since this is a more robust diagnostic. One of the problems in determining line bisectors is the absence of a continuum window in the spectra.

The Doppler shift of the line core was determined from the analytical minimum of a second order polynomial fitted to 5 pixels (0.044 Å) centered at line minimum. At this noise level, this results in an uncertainty of approximately 120 $\mathrm{m\,s^{-1}}$.

The Mn I 3924 line had to be treated with special care: this line is weak and very close to a Ni I line which made the Doppler shift determination difficult. This line was included in the analysis anyway since from this sample it is the line that is formed in the deepest layers of the atmosphere. Spatial locations where no shift could be determined were left out of the analysis. Note the noisy appearance of the Doppler map (Fig. 14a).

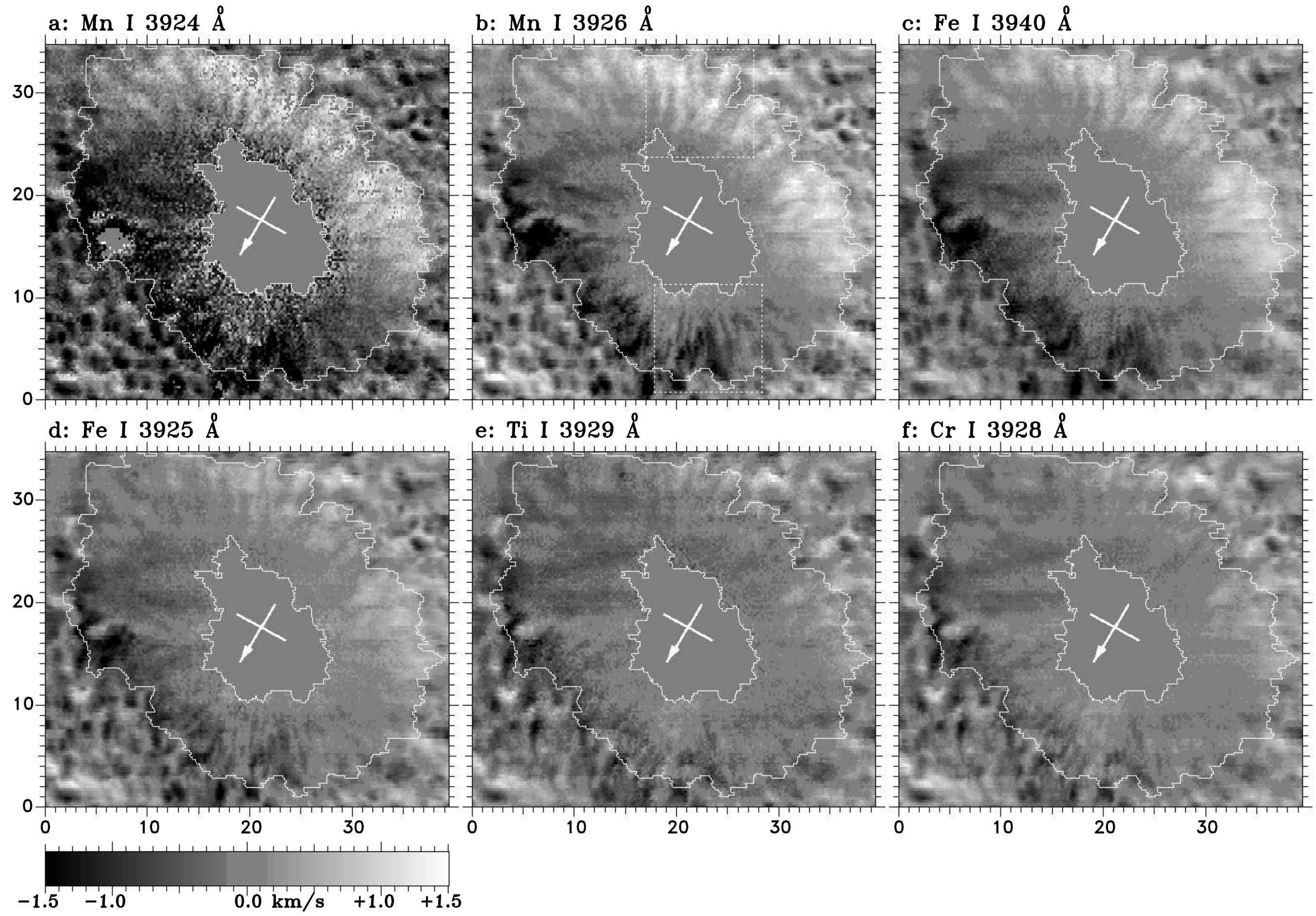

Fig. 14. Doppler maps for lines in order of increasing mean height of formation, ordered from left to right, top to bottom. The umbra has been masked out. The arrow points towards disk-centre. Dark (negative) denotes blueshift. The two squares outlined by dotted lines in the Doppler map for Mn I 3926 (b) mark the areas shown as close-ups in Fig. 16.

The mean position of the line core in the umbral region was used as reference wavelength to calibrate the line-core shifts. The spectra from the umbral region were clearly dominated by scattered light of which a significant fraction originates from the penumbra. By taking the mean line-core position, contributions from centre-side (blue shifted) and limb-side (red shifted) penumbra cancel out.

6.4. Results

The Doppler maps shown in Fig. 14 display a number of well-established observational facts related to the Evershed effect:

1. The division of the sunspot penumbra due to line-of-sight effects: the limb-side penumbra hosts an outflow away from the observer resulting in a red-shift of the line cores while in the centre-side penumbra the line-of-sight velocities are effectively towards the observer resulting in blue-shifted line-cores.
2. The Doppler maps in Fig. 14 have been placed in order of increasing line-core formation height. Comparing the maps it is clear that the measured velocities decrease with increasing formation height. Figure 15 gives a quantitative representation of the measured velocities.
3. The Evershed signal becomes stronger towards the outer penumbra. In general, the strongest velocities are measured near the outer penumbral boundary.

Note that horizontal streaks, notably present in the maps displaying weaker Evershed signals, can be attributed to varying seeing conditions. Since the slit direction is along the horizontal axis, series of spectrograms under less favourable seeing conditions will stand out as horizontal streaks. The Doppler map for Fe I 3937 is not shown since it is similar to the Cr I 3928 Doppler map: the Evershed signal is very weak.

The Evershed effect seems to be concentrated in filamentary structures: at a number of locations the flow is confined to narrow channels. In Fig. 16, close-ups of two regions in the Mn I 3926 Doppler map where the flow channels stand out most clearly are shown with corresponding intensity maps. Careful comparison of the Doppler and intensity maps using blinking techniques on a computer display reveals that most of these flow channels coincide with dark filaments.

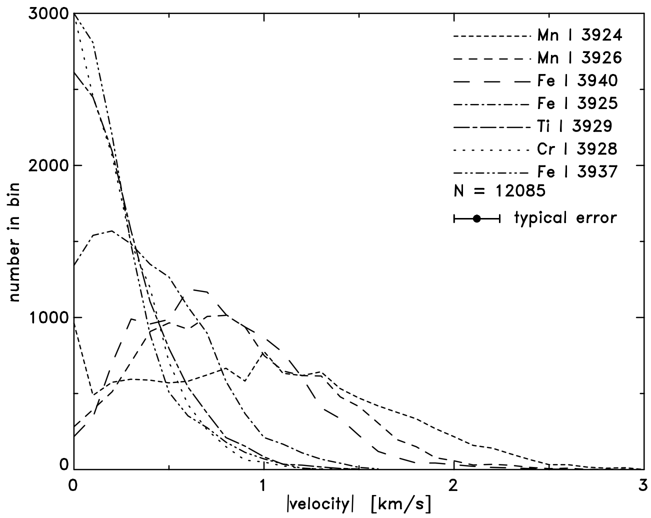

Fig. 15. Histograms of the Doppler shifts for the different lines, measured in 120°wide azimuthal slices, centered on centre and limb-side penumbra. Assuming a radial outflow, the velocities were corrected for LOS effect.

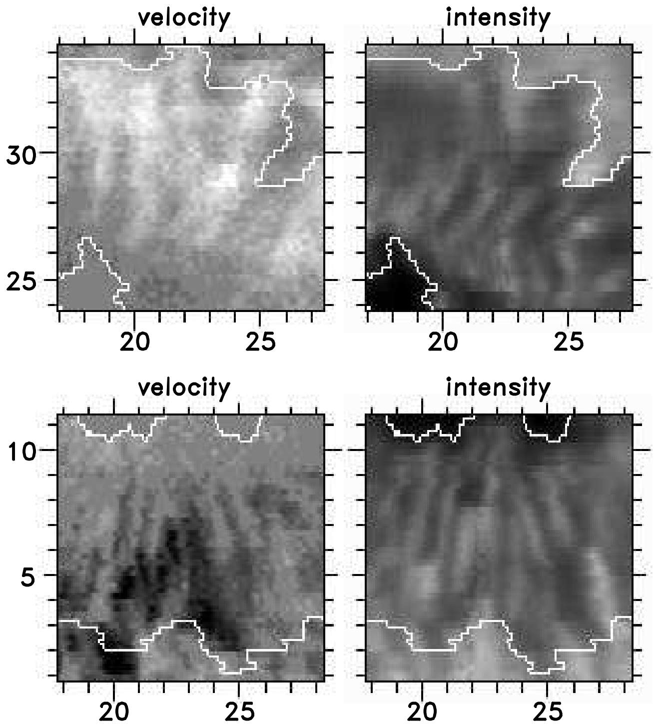

Fig. 16. Close-ups of two Dopplermap-intensitymap pairs. Left are velocity maps from the line-core shift of the Mn I 3926 line (gray-scaled between -1.5 and 1.5 km s^{-1}, like Fig. 14), right intensity in the far Ca II K wing (~ 3924 Å). Coordinate labels in arcseconds matching coordinate system in the Doppler maps in Fig. 14.

To elaborate on this relation in a more quantitative way, Fig. 17 shows cuts through the Mn I 3926 Doppler map and intensity map along azimuthal slices, 120° in angular extent and centered on limb-side and centre-side penumbra respectively. Intensity is measured in the far Ca II K wing and relative to the quiet sun intensity, taken from slit positions well outside the sunspot. This azimuthal path runs through the mid-penumbra, cutting several flow channels. Given the relative measure of a filament being bright or dark, a box-car smoothed local mean (box size 5″) was used as a criterion to distinguish between bright and dark features (see also Schmidt & Schlichenmaier 2000). Although this method is not completely successful for weak intensity variations on small scales, it correctly identifies the nature of most structures. There is a clear trend of dark structures hosting stronger flows but the relationship is not exclusive. Some bright structures contain strong flows and even where the flow is weak it is still clearly present.

It should be noted that the data presented here is essentially a snapshot of the penumbral conditions at one moment in time. Although the Evershed effect is the dominant mechanism for shifting spectral lines, there are other dynamical processes acting that contribute to the net Doppler shift. *P*-mode oscillations may contribute up to several hundred m s^{-1} and there are suggestions that there is an upward component of convective origin ranging up to a few hundred m s^{-1} (Shine et al. 1994). Furthermore, there is evidence that the Evershed effect is temporal in nature with peak-to-peak modulation of 1 km s^{-1} (Shine et al. 1994; Rimmele 1994). All these contributions are impossible to disentangle in a single snapshot but could account at least partly for the velocity signal observed in bright structures.

6.5. Elevated Evershed channels

Rimmele (1995) reported observational evidence of Evershed channels being elevated above the continuum. The evidence was based on a combination of Doppler shift measurements of a set of spectral lines; the C I 5380 line, formed close to the bottom of the photosphere, and the Fe I 5691 line, formed considerably higher in the atmosphere. Dot-like structures in the C I 5380 velocity maps were found to be located at the endpoints of velocity channels observed in Fe I 5691 and were identified as the foot points of the magnetic loops carrying the Evershed flow. In C I 5380, no enhanced velocity signal was found at the location of the Fe I 5691 velocity channels. From this it was concluded that the flow channels are elevated above the continuum.

Rimmele (1995) performed a test of a flow channel of 100 km width and velocity amplitude of 4 km s^{-1} elevated at a fixed height in the HSRA photospheric model. This simple model could reproduce the observed penumbral Fe I 5576 bisectors in a qualitative manner for channel centre elevation heights of 110 and 200 km for centre-side and limb-side penumbra respectively.

Stanchfield et al. (1997) confirmed this observation using the same C I 5380 line and the Fe I 6302.5 line. From inversions of spectropolarimetric data, Westendorp Plaza et al. (2001a) found significant velocities at the $\tau_{5000} = 1$ level only in the inner penumbra. In the higher atmo-

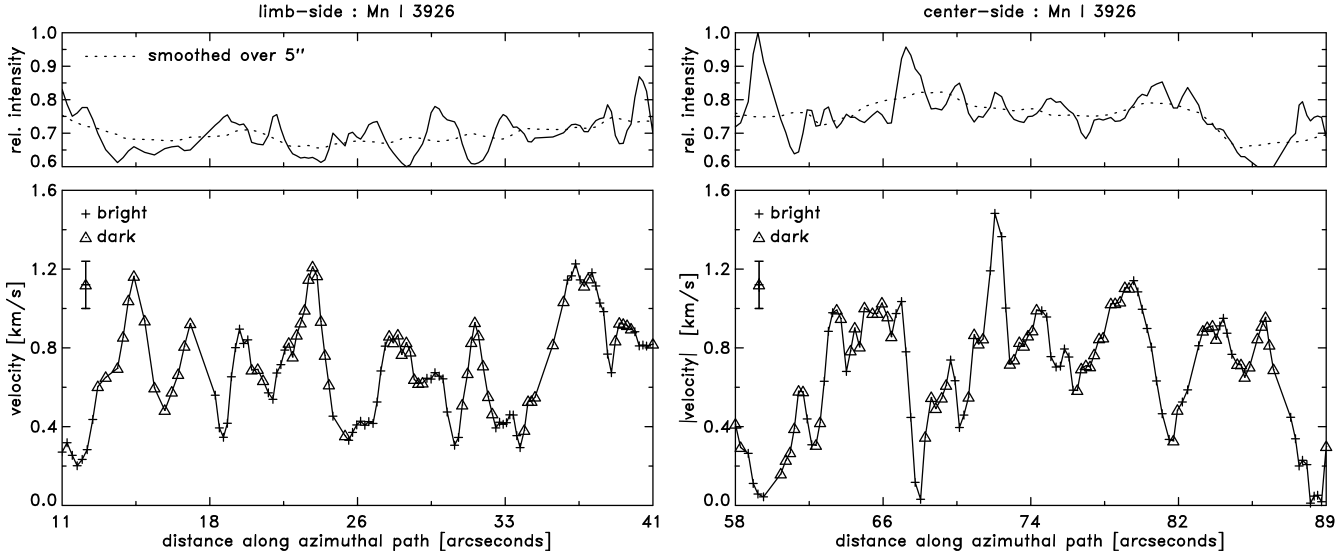

Fig. 17. Evershed flow in bright and dark penumbral structures. Top panels show "continuum" intensity (i.e., in the far Ca II K wing) relative to quiet sun along azimuthal paths through the mid-penumbra. The paths span 120° in azimuthal direction, centered on the limb-side (left) and centre-side (right) penumbra. The dotted line is a 5″–smoothed local mean used as a criterion for defining dark and bright structures. In the bottom panel, showing velocity as determined from the line-core shift of Mn I 3926, these bright and dark structures are marked with crosses and triangles respectively. A typical error bar is given at left.

spheric layers the velocity signal increases with radial distance from spot centre. This was interpreted as the sign of velocity channels that are elevated above the continuum.

In the Doppler maps shown in Fig. 14, there is no sign of such upflow patches. The Doppler map of the lowest formed line, Mn I 3924, harbours the strongest velocities, and despite its noisy appearance, flow channels can be recognized. This sets a limit to the extent of the flow channels being elevated above the continuum which is further scrutinized in the following section.

6.6. A simple flow channel model

In order to investigate different Evershed flow scenarios, a number of tests were performed and compared with the observations. Flow channels of different width and flow speed were released in the cold penumbral atmosphere C at different heights. The line-core Doppler shift was determined for an observing angle of $\mu = 0.77$ and an instrumental profile with an equivalent width of 2 $\mathrm{km\,s^{-1}}$. A spatial resolution element of $0\farcs3$ was adopted and the effective volume occupied by the channel was computed accordingly. To keep the number of free parameters as low as possible, the horizontal and vertical extent of the channel were taken to be the same.

The experiments showed that an individual channel with a width of 50 km, compatible with the siphon-flow and moving-tube models, is too small to give rise to typical observed velocities. A collection of small tubes or one larger tube is needed to be compatible with the observations.

For any channel width larger than 50 km and for any photospheric channel height, line-of-sight velocities that are larger than approximately 6 $\mathrm{km\,s^{-1}}$ affect the line profile too far in the wings to result in a significant line core shift. Velocities of the order of 10 $\mathrm{km\,s^{-1}}$, values that are reached in certain dynamical stages of the moving-tube simulation, cannot be the typical velocity of the bulk of Evershed channels.

Figure 18 summarizes a series of experiments that result in the most reasonable reproduction of the observations. For a channel of width 200 km, the line-core Doppler shifts are plotted as function of height of the channel centre in the penumbral atmosphere. This channel starts to be elevated above the continuum ($z = 0$ km) for centre heights above 100 km. The flow channel contains a horizontal velocity of 5 $\mathrm{km\,s^{-1}}$, resulting in a line-of-sight velocity of 3.2 $\mathrm{km\,s^{-1}}$. Channel centre heights of less than 150 km result in typically observed velocity values (compare with Fig. 15). For centre heights higher than 200 km the velocity set is inverted: the lines formed higher have larger line-core shifts than the lines formed lowest. This is not observed anywhere in the penumbra. This cannot exclude the existence of individual small channels reaching heights of 300–400 km, like in the siphon-flow model, since such small channels barely affect the line-core shift. The bulk of the flow, however, must be concentrated in the lower layers of the penumbral atmosphere.

The basic property of a typical channel being elevated at all cannot be rejected nor confirmed from this simple experiment. The set of spectral lines cores is not reaching deep enough to probe the region under the channels. From these experiments and considering the width of the con-

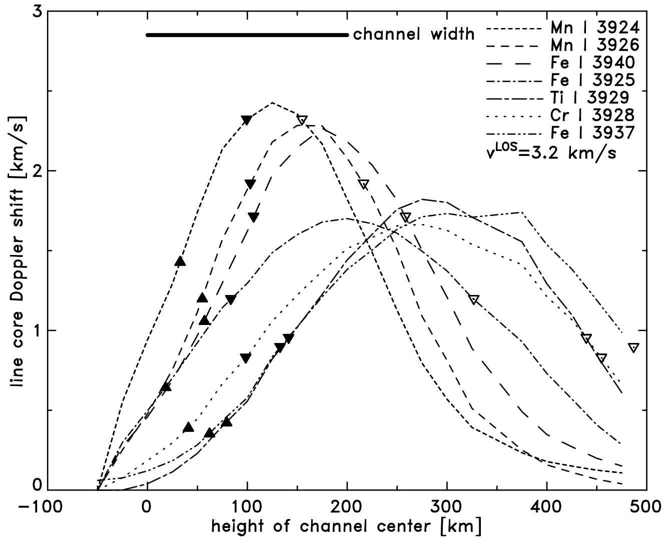

Fig. 18. Line-core Doppler shifts of the line blends as a function of height of a flow channel with a width of 200 km and a flow velocity of 5 km s^{-1} observed under an observing angle of $\mu = 0.77$. The flow channel is released in the cold penumbral atmosphere C. For each line, triangles pointing downward (upward) mark the maximum velocity of 99% (75%) of the observed penumbral velocities. The filled triangles point out that the left part of the curves give a realistic reproduction of the observations, i.e., channel heights around 100 km can account for all observed velocities.

tribution function for Mn I 3924, it can be concluded that where the Evershed channels are observed, the flow must reach at least as deep as 50 km above the continuum.

7. Summary and conclusions

High-spatial-resolution spectra of the Ca II K line were used to derive the temperature stratification of penumbral fine structure and to study the Evershed effect. The results can be summarized as follows:

1. Three semi-empirical atmosphere models, a cool, hot and mean model, were selected as being representative for the temperature stratification of penumbral fine structure. These models agree well with previously published models.
2. Bright (hot) structures have a larger temperature difference between the bottom and the top of the photosphere than dark (cool) structures.
3. In general, penumbral structures keep their relative brightness identity with respect to their local surroundings, i.e., bright (dark) structures in the lower photosphere remain bright (dark) in the upper photosphere. Notable exceptions were found like structures standing out particularly bright in the inner Ca II K wing or the Ca slit-jaw filtergram that were not outstanding with respect to their local surroundings in the lower photosphere (i.e., outer wing).
4. Mean temperature stratifications of limb and centre-side penumbra display an asymmetry in the higher photosphere: the centre-side penumbra is up to 50 K hotter than the limb-side. Hot structures, primarily found near the outer penumbral boundary, are more numerous on the centre-side penumbra and can account for this asymmetry. It is suggested that in bright structures, the isotherms in the higher photosphere have a tilt angle of approximately 7° with the horizontal, pointing downward toward the outer penumbral boundary. This results in a difference in the observing angle between the centre-side and limb-side penumbral that corresponds to a 50 K temperature difference in the inner Ca II K wing.
5. Part of the Evershed signal in Doppler maps of line blends in the Ca II K wing is confined to narrow channels. Close examination of Doppler map and intensity map pairs revealed that most of these channels are associated with dark filaments. There is a general trend of the Evershed signal being concentrated to dark structures, but bright structures with a significant Evershed signal do exist.
6. For the spectral lines used for this study, the mean height of formation on an optical depth scale is not dramatically different when comparing a cool and a hot penumbral structure.
7. From simple numerical tests of flow channels with characteristics that are compatible with theoretical models it was found that:
   - A flow channel or an ensemble of narrow channels must have a width of the order of 200 km.
   - The bulk of the flow must have a velocity not higher than approximately 6 km s^{-1}.
   - The bulk of the flow must be concentrated to heights below 200 km.
8. There is no direct evidence of Evershed channels being elevated above the continuum: the deepest formed line, Mn I 3924, shows the strongest Evershed signal and shows filamentary structure in the Doppler map. Considering the width of the contribution function for Mn I 3924 and the flow channel experiments, the Evershed channels reach down to at least 50 km above the continuum.

The observational results of this study touches upon different aspects of the structure of the penumbra including the Evershed effect. A complete understanding of the penumbra calls for detailed forward modelling with observational findings like these as guideline and touchstone.

Acknowledgements. The author is indebted to D. Kiselman for his support and comments on the manuscript. The helpful comments and support of G. Scharmer are highly appreciated. The author wishes to thank the SVST staff: R. Kever, G. Hosinsky, P. Armas, and I. Hosinsky for their assistance during the observations. The outstanding technical support of W. Wei and P. Dettori is gratefully acknowledged. B. Edvardsson and M. Carlsson are thanked for valuable discussions regarding spectral line formation. The author is grateful to U. Litzén for providing the unpublished Mn I laboratory spectra to estimate the effect of hyperfine splitting. The Crafoord fund of the

Royal Swedish Academy of Sciences facilitated the purchase of a Kodak MegaPlus 1.6 BluePlus CCD camera.

References

Ayres, T. & Linsky, J. 1975, ApJ, 200, 660

Ayres, T., Linsky, J., & Shine, R. 1974, ApJ, 192, 93

Balthasar, H., Sütterlin, P., & Collados, M. 2001, Astron. Nachr., 322, 367

Barklem, P. S., Anstee, S. D., & O'Mara, B. J. 1998, Publ. Astr. Soc. Australia, 15, 336

Barklem, P. S. & O'Mara, B. J. 1998, MNRAS, 300, 863

Barklem, P. S., Piskunov, N., & O'Mara, B. J. 2000, A&AS, 142, 467

Beckers, J. M. 1968, Sol. Phys., 3, 258

Brault, J. & Neckel, H. 1987, Hamburg Observatory anonymous ftp: ftp.hs.uni-hamburg.de

Brault, J. W. & White, O. R. 1971, A&A, 13, 169

Carlsson, M. 1986, Uppsala Astronomical Observatory Report No. 33

Degenhardt, D. 1993, A&A, 277, 235

Del Toro Iniesta, J. C., Tarbell, T. D., & Cobo, B. R. 1994, ApJ, 436, 400

Denker, C. 1998, Sol. Phys., 180, 81

Evershed, J. 1909, MNRAS, 69, 454

Fuhr, J., Martin, G., & Wiese, W. 1988, J. Phys. Chem. Ref. Data 17, Suppl. 3

Gingerich, O., Noyes, R. W., Kalkofen, W., & Cuny, Y. 1971, Sol. Phys., 18, 347

Gray, D. F. 1978, Sol. Phys., 59, 193

—. 1992, The observation and analysis of stellar photospheres (Cambridge University Press)

Grevesse, N. & Sauval, A. J. 1998, Space Sci. Rev., 85, 161

Grossmann-Doerth, U. & Schmidt, W. 1981, A&A, 95, 366

Holweger, H. & Müller, E. A. 1974, Sol. Phys., 39, 19

Johannesson, A. 1993, A&A, 273, 633

Kiselman, D. 1994, A&AS, 104, 23

Kjeldseth Moe, O. & Maltby, P. 1974, Sol. Phys., 36, 101

Kupka, F., Piskunov, N., Ryabchikova, T. A., Stempels, H. C., & Weiss, W. W. 1999, A&AS, 138, 119

Kurucz, R. 1993, Kurucz CD-ROM No. 18. Cambridge, Mass.: Smithsonian Astrophysical Observatory, 1993.

—. 1994a, Kurucz CD-ROM No. 20. Cambridge, Mass.: Smithsonian Astrophysical Observatory, 1994.

—. 1994b, Kurucz CD-ROM No. 22. Cambridge, Mass.: Smithsonian Astrophysical Observatory, 1994.

—. 1994c, Kurucz CD-ROM No. 21. Cambridge, Mass.: Smithsonian Astrophysical Observatory, 1994.

Lites, B. W., Rutten, R. J., & Berger, T. E. 1999, ApJ, 517, 1013

Lites, B. W., Skumanich, A., & Scharmer, G. B. 1990, ApJ, 355, 329

Litzén, U. 2001, private communication

Magain, P. 1986, A&A, 163, 135

Maltby, P. 1997, in ASP Conf. Ser. 118: Advances in Physics of Sunspots, 91

Martin, G., Fuhr, J., & Wiese, W. 1988, J. Phys. Chem. Ref. Data 17, Suppl. 3

Martínez Pillet, V. 2000, A&A, 361, 734

McIntosh, P. S. 1990, Sol. Phys., 125, 251

Meyer, F. & Schmidt, H. 1968, Z. Angew. Math. Mech., 48, 218

Montesinos, B. & Thomas, J. H. 1997, Nature, 390, 485

Muller, R. 1992, in NATO ASIC Proc. 375: Sunspots. Theory and Observations, 175

Nave, G., Johansson, S., Learner, R. C. M., Thorne, A. P., & Brault, J. W. 1994, A&AS, 94, 221

Neckel, H. 1999, Sol. Phys., 184, 421

Neckel, H. & Labs, D. 1984, Sol. Phys., 90, 205

Piskunov, N., Kupka, F., Ryabchikova, T. A., Weiss, W. W., & Jeffery, C. S. 1995, A&AS, 112, 525

Rimmele, T. 1994, A&A, 290, 972

—. 1995, A&A, 298, 260

Ryabchikova, T., Piskunov, N., Stempels, H., Kupka, F., & Weiss, W. 1999, Physica Scripta, T83, 162

Sánchez Almeida, J. 1998, ApJ, 497, 967

Sánchez Almeida, J. & Bonet, J. A. 1998, ApJ, 505, 1010

Sütterlin, P. 2001, A&A, 374, L21

Scharmer, G. B. & Löfdahl, M. G. 1991, Adv. Space Res., 11, 129

Scharmer, G. B., Pettersson, L., Brown, D. S., & Rehn, J. 1985, Aplied Optics, 24, 2558

Schlichenmaier, R. & Collados, M. 2002, A&A, 381, 668

Schlichenmaier, R., Jahn, K., & Schmidt, H. U. 1998a, ApJ, 493, L121

—. 1998b, A&A, 337, 897

Schmidt, W. & Schlichenmaier, R. 2000, A&A, 364, 829

Shand, M., Wei, W., & Scharmer, G. 1995, in SPIE Proc., Vol. 2607, 145

Shchukina, N. & Trujillo Bueno, J. 2001, ApJ, 550, 970

Shine, R. A. 1990, ANA : http://ana.lmsal.com/

Shine, R. A. & Linsky, J. L. 1974, Sol. Phys., 37, 145

Shine, R. A., Title, A. M., Tarbell, T. D., et al. 1994, ApJ, 430, 413

Sobotka, M. 1997, in ASP Conf. Ser. 118: Advances in Physics of Sunspots, 155

Sobotka, M. & Sütterlin, P. 2001, A&A, 380, 714

Solanki, S. K. 2001, in: Encyclopedia of Astronomy and Astrophysics (Nature Publishing Group), 3177

Stanchfield, D. C. H., Thomas, J. H., & Lites, B. W. 1997, ApJ, 477, 485

Theodosiou, C. E. 1989, Phys. Rev. A, 39, 4880

Thomas, J. H. 1994, in NATO ASIC Proc. 433: Solar Surface Magnetism, 219

Title, A. M., Frank, Z. A., Shine, R. A., et al. 1993, ApJ, 403, 780

Vernazza, J., Avrett, E., & Loeser, R. 1981, ApJS, 45, 635

Westendorp Plaza, C., del Toro Iniesta, J. C., Ruiz Cobo, B., & Martínez Pillet, V. 2001a, ApJ, 547, 1148

Westendorp Plaza, C., del Toro Iniesta, J. C., Ruiz Cobo, B., et al. 2001b, ApJ, 547, 1130

Wiehr, E. 1999, in ASP Conf. Ser. 184: Magnetic Fields and Oscillations, 86

Wiehr, E. & Stellmacher, G. 1989, A&A, 225, 528